Geophysical Journal International

Geophys. J. Int. (2015) **200,** 1503–1522 doi: 10.1093/gji/ggu475

GJI Marine geosciences and applied geophysics

Seismic velocity structure and deformation due to the collision of the Louisville Ridge with the Tonga-Kermadec Trench

W. Stratford,[1,*] C. Peirce,[1] M. Paulatto,[2] M. Funnell,[1] A. B. Watts,[2] I. Grevemeyer[3] and D. Bassett[2]

[1] *Department of Earth Sciences, Durham University, Durham* DH1 3LE, *United Kingdom. E-mail: wandastratford@gmail.com*

[2] *Department of Earth Sciences, Oxford University, Oxford* OX1 3AN, *United Kingdom*

[3] *GEOMAR, Helmholtz Centre of Ocean Research, D-*24148 *Kiel, Germany*

Accepted 2014 December 10. Received 2014 December 9; in original form 2013 November 29

SUMMARY

New marine geophysical data recorded across the Tonga-Kermadec subduction zone are used to image deformation and seismic velocity structures of the forearc and Pacific Plate where the Louisville Ridge seamount chain subducts. Due to the obliquity of the Louisville Ridge to the trench and the fast 128 mm yr^{-1} south–southwest migration of the ridge-trench collision zone, post-, current and pre-seamount subduction deformation can be investigated between 23°S and 28°S. We combine our interpretations from the collision zone with previous results from the post- and pre-collision zones to define the along-arc variation in deformation due to seamount subduction. In the pre-collision zone the lower-trench slope is steep, the mid-trench slope has ∼3-km-thick stratified sediments and gravitational collapse of the trench slope is associated with basal erosion by subducting horst and graben structures on the Pacific Plate. This collapse indicates that tectonic erosion is a normal process affecting this generally sediment starved subduction system. In the collision zone the trench-slope decreases compared to the north and south, and rotation of the forearc is manifest as a steep plate boundary fault and arcward dipping sediment in a 12-km-wide, ∼2-km-deep mid-slope basin. A ∼3 km step increase in depth of the middle and lower crustal isovelocity contours below the basin indicates the extent of crustal deformation on the trench slope. At the leading edge of the overriding plate, upper crustal *P*-wave velocities are ∼4.0 km s^{-1} and indicate the trench fill material is of seamount origin. Osbourn Seamount on the outer rise has extensional faulting on its western slope and mass wasting of the seamount provides the low V_p material to the trench. In the post-collision zone to the north, the trench slope is smooth, the trench is deep, and the crystalline crust thins at the leading edge of the overriding plate where V_p is low, ∼5.5 km s^{-1}. These characteristics are attributed to a greater degree of extensional collapse of the forearc in the wake of seamount subduction. The northern end of a seismic gap lies at the transition from the smooth lower-trench slope of the post-collision zone, to the block faulted and elevated lower-trench slope in the collision zone, suggesting a causative link between the collapse of the forearc and seismogenesis. Along the forearc, the transient effects of a north-to-south progression of ridge subduction are preserved in the geomorphology, whereas longer-term effects may be recorded in the ∼80 km offset in trench strike at the collision zone itself.

Key words: Controlled source seismology; Subduction zone processes; Volcanic arc processes; Crustal structure.

1 INTRODUCTION

High convergence rates and a rapid south–southwest migrating collision zone (Lonsdale 1986; MacLeod 1994) make the Tonga-Kermadec Trench–Louisville Ridge collision zone an ideal location to study the effect of seamount subduction on lithospheric structure. Here a major change in tectonic regime in the backarc, a lateral offset in the trench (Ruellan *et al.* 2003), and a zone of elevated and deformed forearc coincide with the subduction of the Louisville Ridge (Bonnardot *et al.* 2007). The seamounts of the ridge exceed 3.5 km in relief above the seafloor and are carried into the

*Now at: GNS Science, Lower Hutt, 5011, New Zealand.

subduction zone at ∼70 mm yr^{-1}, one of the highest global rates of subduction (DeMets *et al.* 1994).

Deformation of the forearc and trench, during and in the wake of subduction of buoyant features, is observed at subduction zones globally (Stern 2011). The two main tectonic erosion processes in a subduction zone are frontal erosion of the overriding plate, and basal erosion, whereby structures on the subducting plate or high pressure fluids released during subduction erode the forearc crust from beneath (Clift & Vannucchi 2004; Stern 2011). Rapid rotation and uplift followed by subsidence of the forearc are attributed to subduction of topographic edifices at a number of subduction systems—for example New Hebrides and Solomon (Taylor *et al.* 2005), Banda Arc (Fleury *et al.* 2009), Costa Rica (Sak *et al.* 2009), Peru (Clift & Pecher 2003) and Cascadia (Trehu *et al.* 2012). These deformation processes may be transient but are recorded in uplifted marine terraces and as differential offsets of forearc blocks on faults at high angles to the trench (Fisher *et al.* 1998). In addition, thickening of the forearc crust by tectonic underplating of subducted forearc material may also occur (Geist *et al.* 1993; Stern 2011).

Once the seamount passes beneath the plate boundary interface, the forearc subsides and undergoes gravitational collapse (Ballance *et al.* 1989; Wright *et al.* 2000; Laursen *et al.* 2002; Taylor *et al.* 2005), with forearc erosion occurring until the pre-seamount subduction forearc taper is re-established (Lallemand *et al.* 1992). Evidence of seamount subduction may be recorded by the rotation of sediment layers in the forearc (Clift *et al.* 1998), as irregularities or indentations in the trench in the wake of seamount subduction (Trehu *et al.* 2012), or as an overall offset in the plate boundary (Lallemand *et al.* 1992; Wright *et al.* 2000; Ruellan *et al.* 2003).

Erosion of the deformed forearc in the wake of seamount subduction is inferred to have caused a ∼80 km offset in the trench north of the current Tonga-Kermadec Trench–Louisville Ridge collision zone (von Huene & Scholl 1991; Lallemand *et al.* 1992; Wright *et al.* 2000). However, the plate boundary as a whole is considered to be an erosive margin (Clift & MacLeod 1999; Clift & Vannucchi 2004). As subduction of the Pacific Plate at the Tonga-Kermadec Trench is fast (DeMets *et al.* 1994) and sediment poor (Heuret *et al.* 2012), tectonic erosion of the overlying plate is inferred to be a general process affecting this plate boundary (Clift & MacLeod 1999). Horst and graben structures formed by bending-induced extension at the outer rise can enhance frontal and basal erosion of the overlying plate, particularly when the trench is sediment starved (von Huene & Scholl 1991; Stern 2011).

To distinguish seamount subduction-related deformation from normal Tonga-Kermadec erosive subduction, the 'before, during and after' regions have been the target of a number of marine geophysical surveys in recent years (Herzer & Exon 1985; Ballance *et al.* 1989; Clift *et al.* 1998; Crawford *et al.* 2003; Contreras-Reyes *et al.* 2011); the most recent being the R/V Sonne cruise SO215 in 2011 (Peirce & Watts 2011). Previous studies have investigated the effect of seamount subduction on the geomorphology of the Tonga-Kermadec subduction zone and have focused on the along-arc changes in seafloor features in the forearc and trench (Clift *et al.* 1998; Wright *et al.* 2000). However, the effects of seamount subduction extend far beneath the surface and studies of the crust and upper mantle are required to fully understand the short-to-long-term effect seamount subduction has on the overriding plate. Here, we describe seismic and density models of the crust and upper mantle in the current seamount collision zone, and compare them to previous seismic studies in the post-collision zone to the north (Contreras-Reyes *et al.* 2011) and the pre-collision zone to the south (Funnell *et al.* 2014) to interpret the along arc variation in deformation associated with the subduction of the Louisville Ridge seamount chain.

2 GEOLOGICAL SETTING

Subduction of the Pacific Plate beneath the Indo-Australian Plate began in the Eocene at the Tonga-Kermadec Trench (Malahoff *et al.* 1982; Sutherland 1999). Plate convergence rates vary from 80 mm yr^{-1} at 17°S to 45 mm yr^{-1} at 39°S (DeMets *et al.* 1994). This seemingly linear, 2000-km-long subduction system is subdivided at its intersection with the Louisville Ridge at 26°S (Fig. 1) into the Tonga Ridge to the north and the Kermadec Ridge to the south. These ridges were formed by arc magmatism during the initial building of the forearc in the Eocene (Bloomer *et al.* 1994; Tappin 1994).

The Tonga Ridge is broad, elevated, flat-topped and capped with sediment and has undergone several extensional collapse events since opening of the Lau Basin began in the late Miocene (Herzer & Exon 1985). In contrast, to the south the Kermadec Ridge is narrow with a forearc basin that contains strata dipping towards the trench. The differences between the ridges have been attributed to either along-arc variation in Miocene post-rifting structure (Parson & Hawkins 1994), or the Tonga Ridge being altered by Louisville Ridge subduction (Dupont & Herzer 1985; Pelletier & Dupont 1990). A decrease in the arc-trench gap beneath the Kermadec Ridge, compared to the Tonga Ridge to the north, may be indicative of an increase in slab dip south of the collision zone (Bonnardot *et al.* 2007).

Predominately of basaltic composition, the ∼4000-km-long Louisville Ridge seamount chain intersects the Tonga-Kermadec Trench at an angle of ∼36°. The ridge is not strictly linear, its track undulates and can be divided into ∼200-km-long segments offset by small changes in strike (Fig. 1, inset). The ridge was formed by the passage of the Pacific Plate over the Louisville Hotspot, which is presently located near the intersection of the Eltanin Fracture Zone with the East Pacific Rise (Lonsdale 1986; Watts *et al.* 1988). Temporal variations in magmatic productivity of the hotspot have been inferred with a general waning with time (Watts *et al.* 1988; Koppers *et al.* 2004). The ridge has been dated from dredge samples and analysis of IODP drilling samples (e.g. Koppers *et al.* (2004); Koppers *et al.* (2012); Expedition 330 Scientists (2012) and its obliquity to the trench is inferred to have been greater in the past, with a decreasing southward progression of ridge subduction rate with time from 283 mm yr^{-1} at 3.5 Ma to the current rate of 128 mm yr^{-1} (Ruellan *et al.* 2003).

In the Lau Basin to the north of the ridge-trench collision zone, backarc spreading occurs in a wedge-shaped area (Weissel 1979; Ruellan *et al.* 1994). To the south, extension occurs in the Havre Trough, convergence rates are slower and the backarc is more rectangular in shape (Fig. 1, inset). This significant change in the style of backarc extension is attributed to the effects of subduction of seamounts on the locking/unlocking of the subduction system (Ruellan *et al.* 2003).

Changes in forearc properties are manifest in a ∼150-km-wide zone of deformation at the ridge-trench collision. In addition, the zone is associated with a region of reduced seismic activity compared to the north and south, especially in shallow and intermediate depth seismicity. Seismic gaps are associated with the fracturing and interplate weakening effects of subducting relief (Wang & Bilek 2014). However, the seismic gap at the Louisville Ridge is wider than the seamount edifices being subducted and is broadly similar

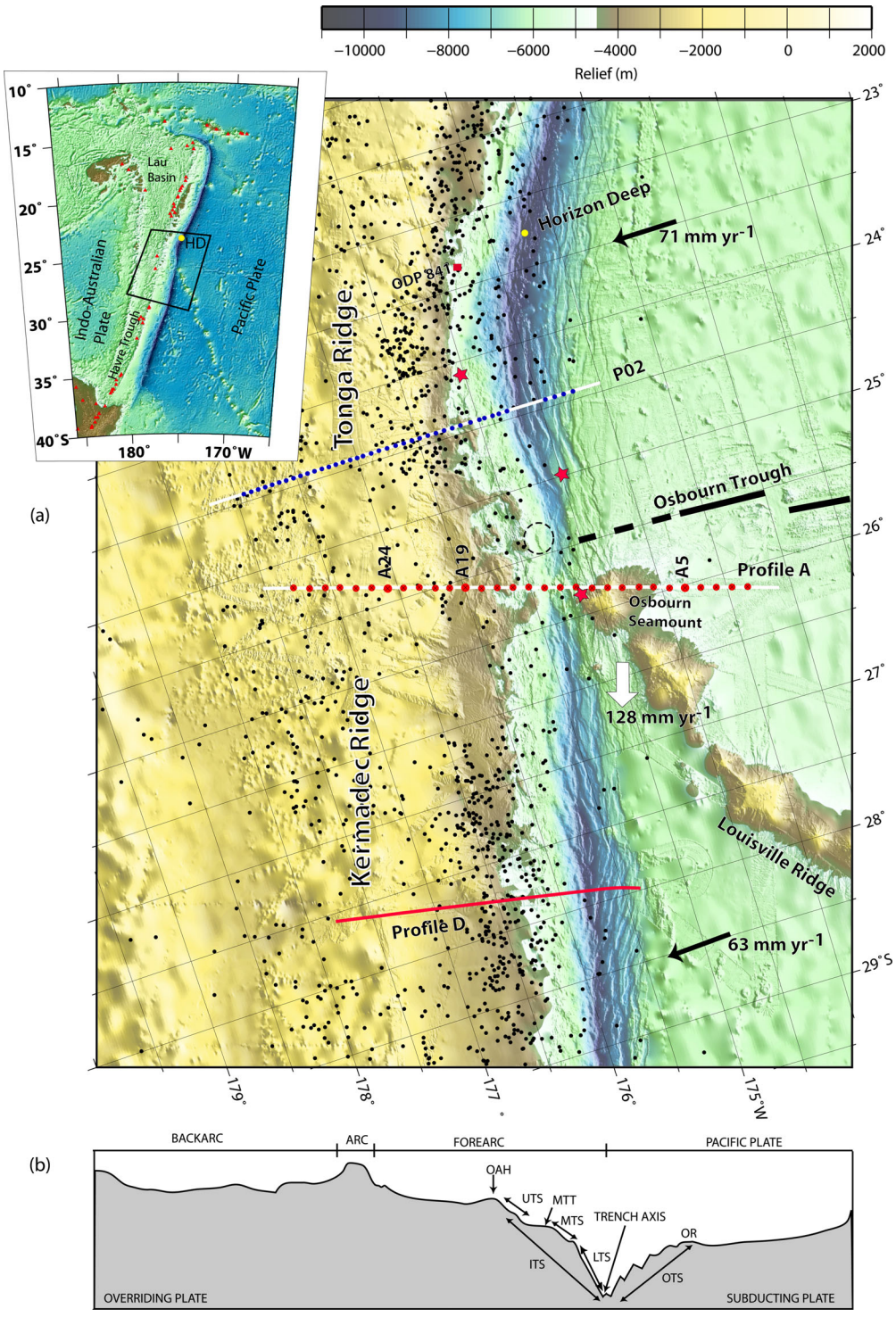

Figure 1. Location of the Tonga-Kermadec subduction system in the SW Pacific. (a) Relief in the study area shown by a 150 m × 150 m resampled compilation grid of ship track bathymetry measurements from recent cruises, and the GEBCO global 30 arcsecond grid (Becker *et al.* 2009). The solid and dashed black line marks Osbourn Trough, which intersects the trench at ∼25.5°S. Profile A (white with red dots for OBS locations) crosses the current collision zone. Additional constraint is provided by Profile P02 (white with blue dots for OBSs locations — (Contreras-Reyes *et al.* 2011) and MCS Profile D (red line) which cross the post- and pre-collision zones in the north and the south respectively. Black arrows give Australian Plate-fixed plate convergence directions and rates (DeMets *et al.* 1994). White arrow shows Tonga-Kermadec Ridge — Louisville Ridge collision zone migration rate. ODP drill site is shown by a red square and black dots show background seismicity for earthquakes $>M_b = 5$. Red stars are $M_b = 7.4$–7.5 earthquakes in the seismic gap. Dashed circle shows the location of the proposed Motuku Seamount of Ballance *et al.* (1989). Inset: The generalized features of the SW Pacific — the Tonga-Kermadec Ridge, the trench and backarc, and the Louisville Ridge which intersects the trench at ∼26°S. The study area (black outline) includes both pre-, current and post-collision lithosphere of both the subducting and overriding plates. HD is Horizon Deep, the deepest part of Tonga Trench. Red triangles are active arc volcanoes. (b) Sketch showing the main components of the subduction system discussed in the text. OAH is outer-arc high, ITS is the inner-trench slope, UTS is the upper-trench slope, MTT is the mid-trench terrace, MTS is the mid-trench slope, LTS is the lower-trench slope, OTS is the outer-trench slope, and OR is the outer rise.

in size to the footprint of the flexural moats flanking the subducting ridge and to the forearc collision zone. The association of the seismic gap with the ridge suggests that the stress state of the overriding plate has been altered by the subducting seamounts and their flexural moats (Bonnardot *et al.* 2007). Three large earthquakes ($M_w = 7.4$–7.5) located in close proximity to the subducting Louisville Ridge have been attributed to near-surface locking effects (Christensen & Lay 1988).

Multichannel seismic reflection data acquired across the collision zone in the late 1980s image an arcward-dipping reflector beneath the lower-trench slope at ~25.5°S (Ballance *et al.* 1989). Ballance *et al.* (1989) associate this reflector with the top surface of a subducted seamount, naming it Motuku (Fig. 1). The inferred seamount is on the same strike as the three oldest Louisville Ridge seamounts and at a similar along-ridge spacing, lying half way between Profile A of SO215 (Peirce & Watts 2011) and Profile P02 (Fig. 1) of an earlier R/V Sonne cruise SO195a (Contreras-Reyes *et al.* 2011).

The ~78 Ma Osbourn Seamount (Clouard & Bonneville 2005; Koppers *et al.* 2012) is currently riding the outer rise seaward (east) of the Tonga-Kermadec Trench and will be the next in the chain to be subducted. The trench floor directly arcward of Osbourn Seamount shallows by 3000 m, compared to just north and south of the collision zone, and comprises a broad zone of faulted blocks. The adjacent forearc is also elevated by ~300 m compared to the forearc to the north. Seabed imaging here reveals a zone of extensive faulting with large-scale mass wasting events forming canyons and sediment pathways across the outer forearc, indicating a region of instability and progressive uplift (Clift *et al.* 1998).

3 MARINE GEOPHYSICAL DATA

Over 1500-line kilometres of geophysical data were acquired during R/V Sonne cruise SO215 (Peirce & Watts 2011). Swath bathymetry, gravity, magnetics, parasound and multichannel seismic (MCS) and wide-angle seismic data were acquired contemporaneously along five profiles. Profile A, presented in this paper (Fig. 1) is a coincident wide-angle and MCS profile that intersects the trench at a high angle, crossing the forearc, trench and Osbourn Seamount at the Louisville Ridge collision zone. All models and seismic profiles presented here are aligned by a common co-ordinate reference system in which 0 km is located at the trench axis and positive model and profile offsets are towards the east.

3.1 MCS data

The primary purpose of the MCS data acquisition was to image layer thicknesses and internal structure in the sedimentary succession along the wide-angle profile to provide constraint to the shallow section of the ray trace model. Twelve Sercel G-guns in two, six-gun subarrays and comprising a total volume of 5440 in^3, were used as the seismic source. This array was carefully tuned for contemporaneous MCS and wide-angle acquisition, and to address the energy scattering and propagation challenges of a thin pelagic sediment cover (Burns *et al.* 1973; Lonsdale 1986; Menard *et al.* 1987; Zhou & Kyte 1992; Heuret *et al.* 2012) and the large and rapid lateral variation in seafloor morphology and relief (Fig. 1). Shots were fired at 60 s intervals (~150 m shot spacing at a surveying speed of 4.5 km) to minimize water-wave wrap-around in the wide-angle data. These shots were recorded using a 3-km-long, 240-channel streamer with a 12.5-m-group interval and towed at ~10 m depth, and resulted in a data fold of ~10.

A simple pre-stack processing sequence was applied including common depth point (CDP) sorting into 25 m bins, normal move-out correction and surface consistent deconvolution. A Butterworth filter (bandpass range: 3–10–100–120 Hz) was used to remove high amplitude sea swell and wave noise. Velocity analysis included velocity picking at a spacing of 10–100 CDPs horizontally (depending on the rate of lateral variability) and 0.1–0.3 s two-way traveltime (TWTT) vertically. Below basement a simple velocity gradient was assumed and extrapolated to the bottom of the record section as no distinct intracrustal primary reflections are observed. To minimize the amplitude of the seafloor multiple, a post-stack deconvolution filter was designed using the primary reflection from a region of smooth, flat-lying seafloor. Post-stack, constant velocity (1.5 km s^{-1}) Kirchhoff migration was applied to reduce the appearance of seabed-scatter diffraction tails. For final section plotting (Fig. 2), a water column mute, mean trace scaling and automatic gain compensation were applied.

3.2 Wide-angle seismic data

Thirty ocean-bottom seismographs (OBSs), each with a hydrophone and a three-component geophone package as sensors, were deployed along Profile A at ~12 km spacing and in water depths of up to 6000 m. Four expendable bathymetric thermographs spread evenly along the profile were deployed contemporaneously with the OBSs and used to determine the water column velocity structure. The resulting velocity–depth profiles were referenced back to a sound velocity profile to 3000 m depth conducted at the start of the cruise to calibrate the swath bathymetry data. As part of record section creation, OBSs were relocated to their correct seafloor position by modelling the arrival times of the water wave and seafloor-sea surface multiple. The final record sections (e.g. Figs 3a, 4a and 5a) can be divided, on the basis of their signal-to-noise ratio (SNR), into three main tectonic regimes—the Tonga Ridge, the trench and the subducting Pacific Plate—and the general characteristics of the data from each of these three regions are discussed below.

3.2.1 Tonga Ridge

OBSs deployed across the Tonga Ridge recorded arrivals to ~100 km shot-receiver offset (Fig. 3a). Sediment arrivals from the forearc (P_s) are observed for ~8 km shot-receiver offset in the west (Fig. 3a), decreasing to 5 km in the east, and crustal diving waves (P_g) are observed from ~5 to 70 km shot-receiver offset (Figs 3b and c). Refracted arrivals from the upper mantle (P_n) are observed at longer offsets (>70 km). Moho reflections (P_mP) are only recorded by OBS A20, most likely due to better coupling at this locality as P_g and P_n arrivals are also observed to greater offsets than elsewhere on the forearc.

3.2.2 Trench

Signal attenuation decreases westward (Fig. 4a) with crustal arrivals observed only over shot-receiver offsets <30 km on OBSs located on the outer trench wall, but increasing to >70 km by the inner trench wall. In the trench, near-offset arrivals are observed but are labelled P_g and not P_s, as distinct sedimentary layers are only observed on the coincident MCS record section at the mid-trench slope (Fig. 2a, offset –75 km). P_n arrivals are observed over shot-receiver offsets of 60–120 km.

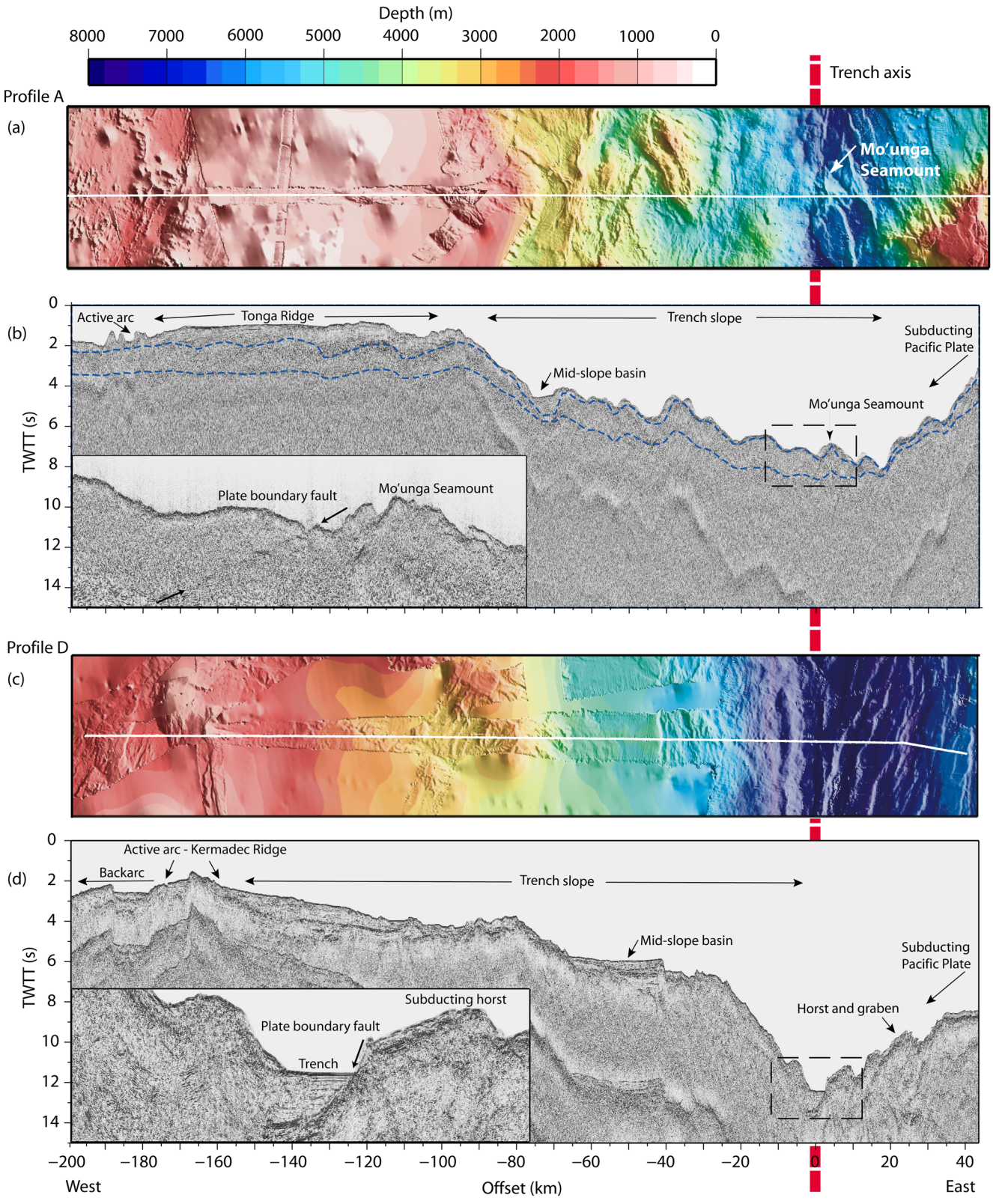

Figure 2. MCS data acquired along Profiles A and D (Funnell *et al.* 2014). (a) Bathymetry along Profile A (white line). (b) Corresponding MCS data. Main plot data is unmigrated. Blue dashed lines are the layer interfaces from the final wide-angle model (Fig. 6a) converted to TWTT. Note the good correlation with MCS reflections. Inset shows the plate boundary fault on the west side of Mo'unga Seamount. Dashed box shows the location of the inset. (c) Bathymetry along Profile D (white line). (d) Corresponding MCS data from (Funnell *et al.* 2014). Note the horst and graben on the outer rise. Inset shows the plate boundary fault and trench axis sediment. Red dashed line on all parts shows the trench axis.

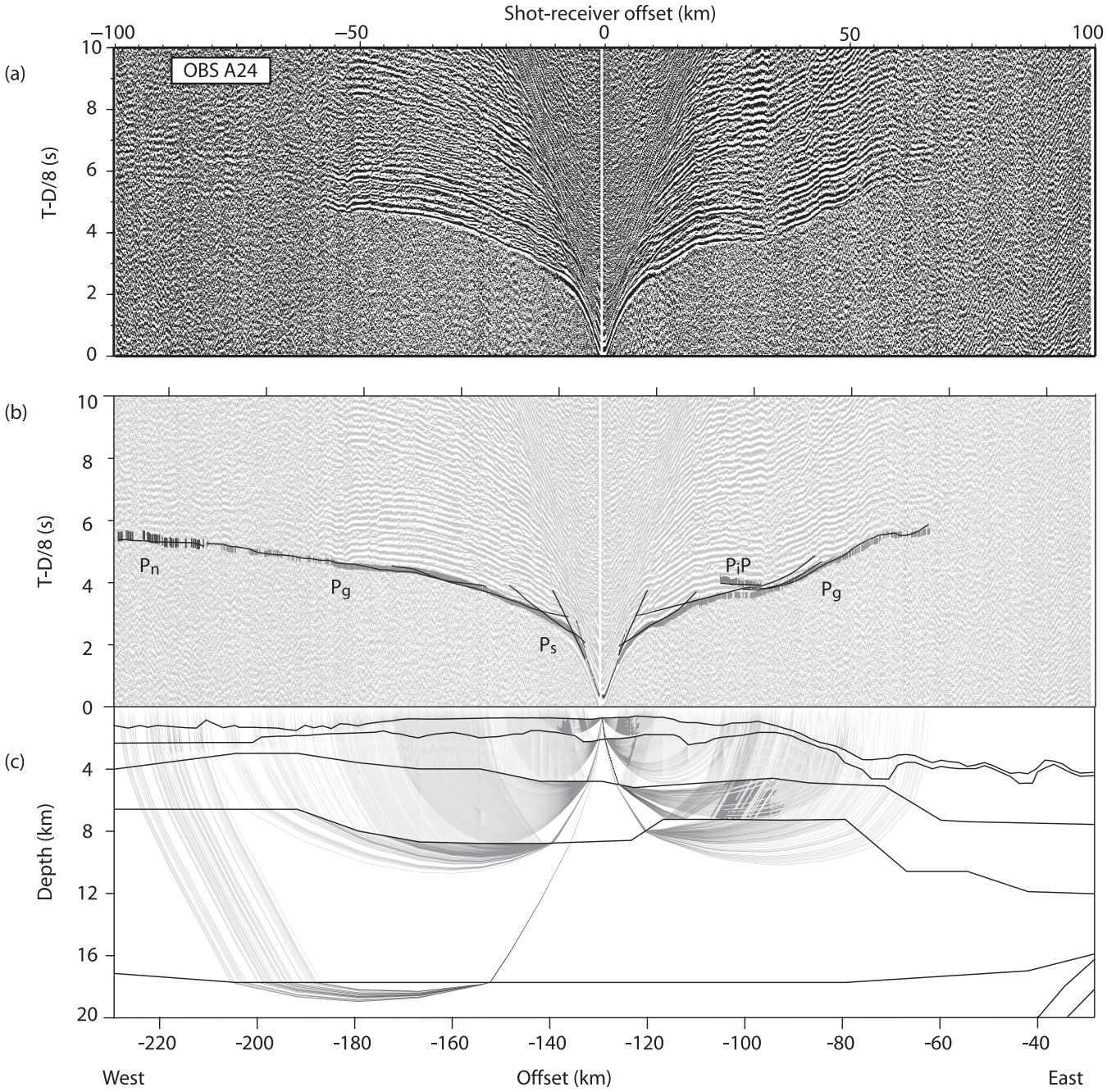

Figure 3. Example forearc record section from OBS A24. See Fig. 1 for location. (a) Data have been bandpass filtered at 2–4–25–40 Hz and deconvolved for display purposes. (b) Comparison of modelled and observed travel-times. Vertical bars are traveltime picks with associated uncertainties and black lines are modelled synthetic arrivals to show the fit to observed arrival times. Picks are overlain on data high-pass filtered above 2 Hz. Main phases are labelled. See Section 3.2 for phase descriptions. (c) Ray diagram for the section of the model covered in (a). Model zero offset coincides with the trench axis and positive offsets are to the east, negative offsets to the west. See text for details.

3.2.3 Pacific Plate

On OBSs located on the flanks of Osbourn Seamount (OBSs A9–A12—Fig. 1), seamount topography produces significant variation in P_g arrival times. P_g arrivals that have propagated through the edifice are observed to ∼4 km shot-receiver offset for OBSs located on the eastern flank, increasing to ∼8 km offset at its centre. Arrivals from the middle crust are observed from ∼4–8 to 40 km offset and an intra-crustal reflection (P_iP) is observed on the eastern side of the seamount (Figs 5c and d). P_n arrivals from beneath the seamount are recorded on the eastern flank OBSs (A4–A9), and in the trench (OBSs A14 and A12). Arrivals from the Moho are observed on the mid-trench slope OBSs (A16–A19) and are recorded in the shot-receiver offset range of 30–40 km for P_mP and 80–120 km for P_n. Most OBSs located on the Pacific Plate recorded P_mP and P_n arrivals at 30–40 km and >40 km offsets, respectively.

3.3 Wide-angle forward modelling

Using stacking velocities, sediment thicknesses and intrasediment interface depths were calculated from the MCS data and used to

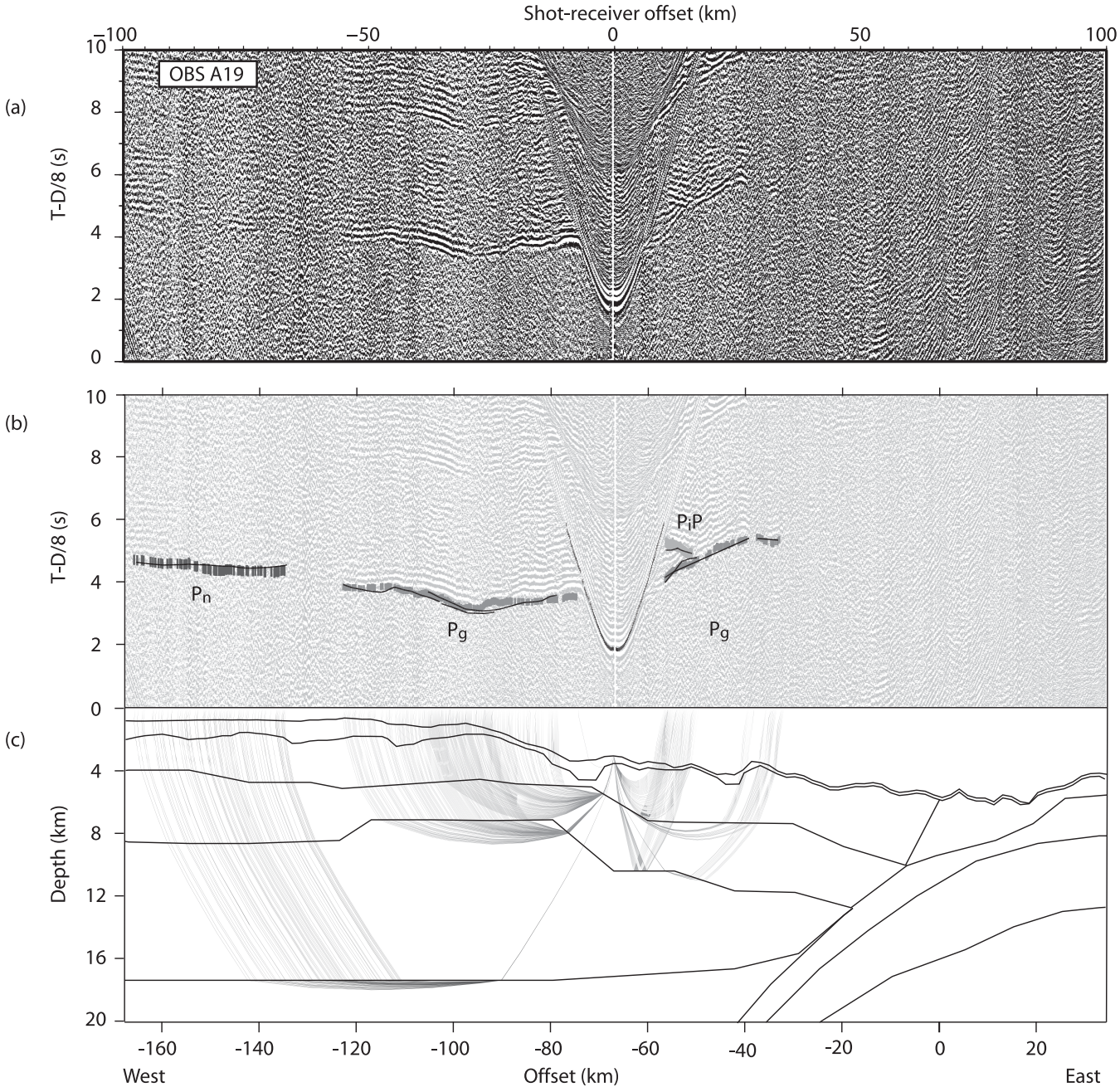

Figure 4. Example inner-trench slope record section from OBS A19. See Fig. 1 for location and Fig. 3 for details.

build the upper part of the initial starting model for wide-angle ray trace modelling. The water column was added using the depth to seabed, and a velocity structure derived from the expendable bathymetric thermographs deployed along the profile.

Forward modelling of *P*-wave arrival times was undertaken using *rayinvr* (Zelt & Smith 1992). In general, first arrival traveltimes were picked from OBS record sections with a 2 Hz high-pass filter applied to remove low-frequency sea swell and wave noise. In regions where low SNR levels hampered arrival picking, a broad bandpass filter (2–4–12–25 Hz) was applied, and these traveltime picks were down-weighted and modelled with larger uncertainties (150 ms). Pick uncertainties were assigned on the basis of SNR, and resulted in location and offset dependent values (see Table 1). Initially only traveltimes picked from high-pass filtered data were included in order to achieve the first-pass fit, before adding those derived from bandpass filtered data (Figs 3–5).

Modelling followed a top-down approach, fitting first the sediment and upper crustal arrivals prior to tracing progressively deeper layers and fitting the longer offset, lower crust and uppermost mantle arrivals. For each layer, the arrivals from a subset of adjacent instruments were modelled simultaneously and a 'rolling window' approach was adopted to extend the fit along the length of the profile.

The fit of calculated arrivals to the traveltime picks (Figs 3–5) was initially qualitatively assessed to produce a model that approximately satisfied the observed data. Subsequently, analysis of rms traveltime misfit and the χ^2 parameter (Zelt & Smith 1992) provided a quantitative assessment and acted as a statistical indicator when making minor adjustments to further refine model fit. A χ^2

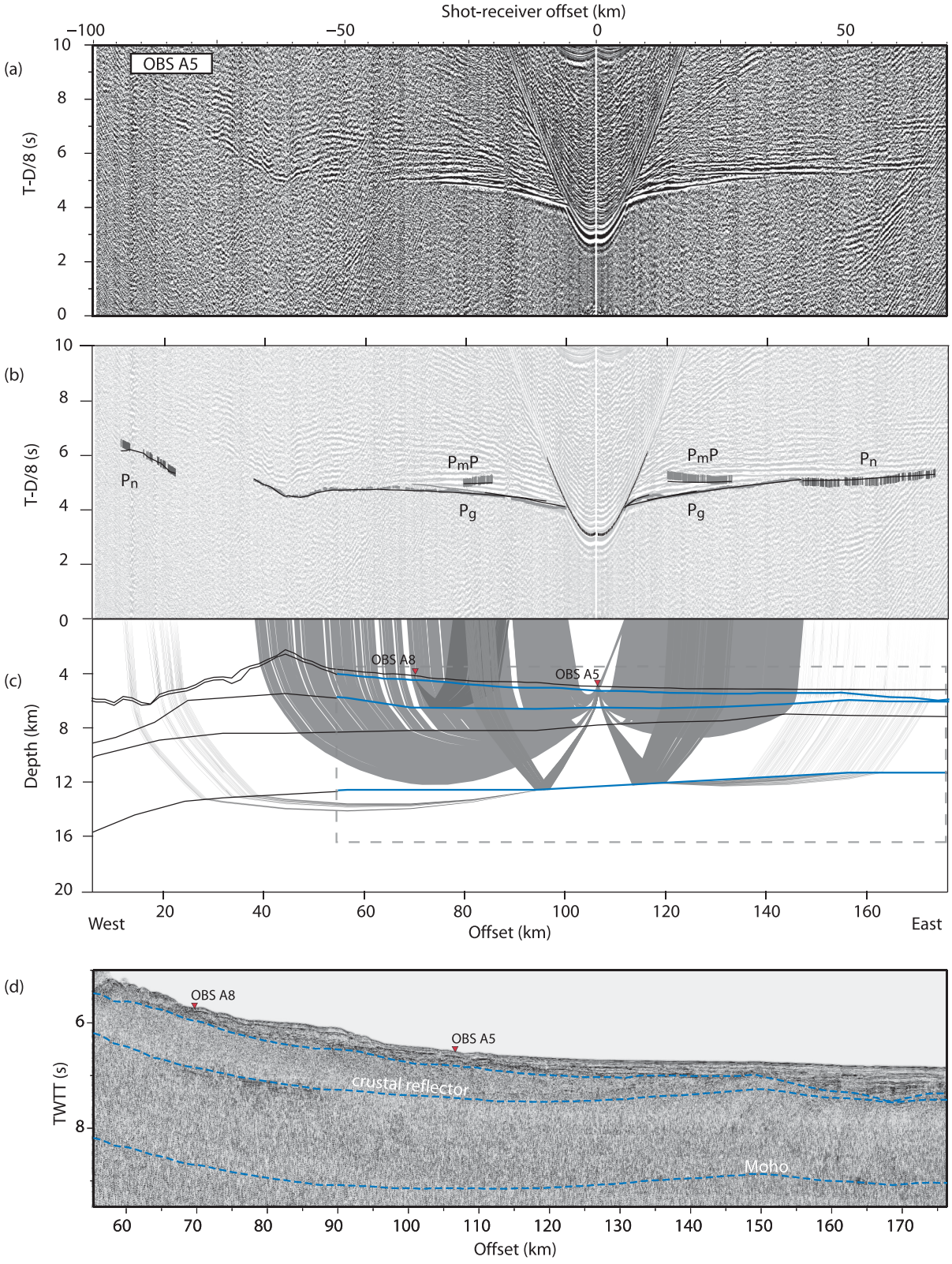

Figure 5. Example Pacific Plate record section from OBS A5. See Fig. 1 for location and Fig. 3 for details for parts (b) and (c). (d) MCS data from the eastern end of Profile A, traversing the eastern flank of Osbourn Seamount and the Pacific Plate. Section location is shown by dashed box on the model in (c). Note the strong crustal reflector beneath the east flank of the seamount, interpreted as the top of oceanic crust prior to seamount loading, that has been blanketed with material originating from the eruption of the seamount at ∼78 Ma. Ray paths for the crustal reflector from OBS A8 are also shown in (c). Moho reflections are observed at the easternmost end of the profile at ∼9 s TWTT. Overlain blue dashed lines are the blue wide-angle model layer interfaces in (c) converted to TWTT.

Table 1. Assigned pick uncertainties and calculated model misfits (rms and χ^2 values): n is number of observations, σ is assigned pick uncertainty, Δt_{rms} is the rms misfit of the model to the picks, and χ^2 is the normalized chi-squared statistic. Normalized χ^2 represents the fit between modelled and observed traveltimes relative to the pick uncertainties. Values less than 1 indicate overfit of the data, and χ^2 values of 1 represent the best obtainable fit. Note that the χ^2 fit for P_n arrivals is less than one. In this case, this reflects the relatively small number of picks rather than a high model certainty at the base of the crust (Table 1). P_g arrivals were assigned an uncertainty of 50 ms for the Pacific Plate, and 100 ms for forearc and trench. As SNR was reduced at longer offsets, deeper travelling phases (P_mP and P_n) were assigned a higher uncertainty of 150 ms.

	n	σ	Δt_{rms}	χ^2
P_s forearc	122	0.1	0.127	1.634
P_g forearc	4942	0.1	0.137	1.877
P_g trench	1542	0.1	0.161	2.587
P_g Osbourn seamount	2491	0.1	0.144	2.081
P_g Pacific Plate	3039	0.05	0.073	2.117
P_mP Pacific Plate	853	0.15	0.158	1.177
P_mP Australian Plate	148	0.15	0.179	1.428
P_n Australian Plate	651	0.15	0.107	0.509
P_n Pacific Plate	1463	0.15	0.125	0.697
P_iP (crustal reflections)	155	0.1	0.138	1.573
Model total	15 402	(0.05–0.15)	0.161	2.294

Table 2. Layer and velocity uncertainties for the wide-angle model.

	ΔZ (km)	ΔV_p (km s^{-1})
Upper and middle crust	0.5	0.05
Lower crust	1	0.1
Forearc Moho (inner)	1	0.1
Forearc Moho (outer 60 km)	2	0.15
Pacific Plate Moho	0.5	0.1

of 1 is considered a good fit, while a χ^2 of <1 is regarded as an overfit to the observed traveltime picks. In this study a χ^2 of <2.6 is considered an acceptable fit.

3.4 Best-fitting model testing

A fit within a χ^2 of <2.6 does not guarantee the uniqueness of the model as an arrival traveltime is dependent not only on seismic velocity but also propagation path length. Consequently, an acceptable fit can be obtained by trade-off of one of these parameters against the other. To estimate the model uncertainties associated with this trade-off, the resolution and uniqueness of the final, best-fitting velocity–depth model were tested by: (i) sensitivity testing; (ii) fit to MCS reflectivity and (iii) gravity modelling.

3.4.1 Sensitivity testing

The final, best-fitting model was sensitivity tested to determine the resolution in depth and geometry of the individual layer boundaries (ΔZ) and the resolution of layer velocities (ΔV_p), whilst still achieving an acceptable fit to within the errors (Table 2). A model was considered an acceptable fit while the rms errors remained within double the pick uncertainty (Table 1) of the layer being tested (Table 2). This approach shows final model velocities are constrained to within ±0.10 km s^{-1} from the seabed to the Moho, except for the outer forearc region where the velocity at the Moho is constrained only to ±0.15 km s^{-1}. Similarly, by varying the depth to and thickness of each layer systematically, testing showed that these parameters are constrained to better than ±1.0 km throughout the model except in the outer forearc region where Moho depth is only resolved to ±2.0 km.

3.4.2 Fit to MCS reflectivity

To compare the final, best-fitting wide-angle model (Fig. 6b) with the MCS data (Fig. 2b), Profile A was reprocessed using a stacking velocity model created by combining the crustal wide-angle velocity model with the velocity picks made from the sediment layers observed in the original MCS data section. Having first resorted and reapplied the geometry for a finer CDP bin interval of 12.5 m, a pre-stack time-migration process was applied and the data restacked. This approach provides a means of testing the non-uniqueness of the forward model, since interface depths and geometries interpreted independently from analysis of both data types should match within the uncertainties of each method. The depths to the interfaces of the final wide-angle model were converted to TWTT and overlain on top of MCS Profile A (e.g. Figs 2b, 5d and 7). Although the lateral resolution of the wide-angle model is lower than that of the MCS data, the TWTT converted interfaces agree within the depth uncertainties (±0.5 km for sedimentary interfaces and crustal reflectors of the Pacific Plate and ±1 km for the Moho) derived from the sensitivity testing.

3.4.3 Gravity modelling

Gravity modelling was used as the final stage of uniqueness testing. This modelling also provided additional constraint on the two areas of the model with sparse ray coverage: (i) the lower crust and Moho of the outer 60 km of the forearc and (ii) the location and dip of the subducted slab beneath the overriding plate (Fig. 6b). The recorded shipboard free-air gravity anomaly (Fig. 6c) was modelled using *grav2d*, a 2-D modelling code based on the polygon approach of Talwani *et al.* (1959). Leaving interface depths unchanged, the velocities from the best-fitting wide-angle model were used to define the framework of the density–depth model. Laterally dividing the layers into additional polygons accommodated significant changes in V_p within a model layer (Fig. 6d). The mean V_p in each polygon was then used to calculate its bulk density using standard velocity–density relationships (Ludwig *et al.* 1970; Brocher 2005).

The gravity anomaly over the Pacific Plate and trench, including the shallow slab position, are fitted with the seismically constrained density model. However, a long wavelength positive signal extends across the forearc and is attributed the subducted Pacific Plate lithosphere beneath the forearc (Figs 6c and d). To model this long wavelength anomaly, the position and dip of the slab from 25 to 300 km depth within the model was defined using other Wadati–Benioff zone seismogenesis studies, coupled with a compilation of slab structures derived from active- and passive-source seismological studies (Bonnardot *et al.* 2007; Hayes *et al.* 2012). Below 100 km the lithospheric mantle of the slab was modelled with a density contrast of 40 kg m^{-3} with the surrounding mantle. This density contrast is a mid-range value for the Pacific Plate at depth at the Tonga-Kermadec subduction system (Billen *et al.* 2003), and used elsewhere to model the subducting Pacific Plate (e.g. Aleutian arc: Watts & Talwani (1974). Densities in the section of the Pacific Plate crust subducted beneath the forearc were also increased by ∼150 kg m^{-3}, in keeping with studies that show a density increase

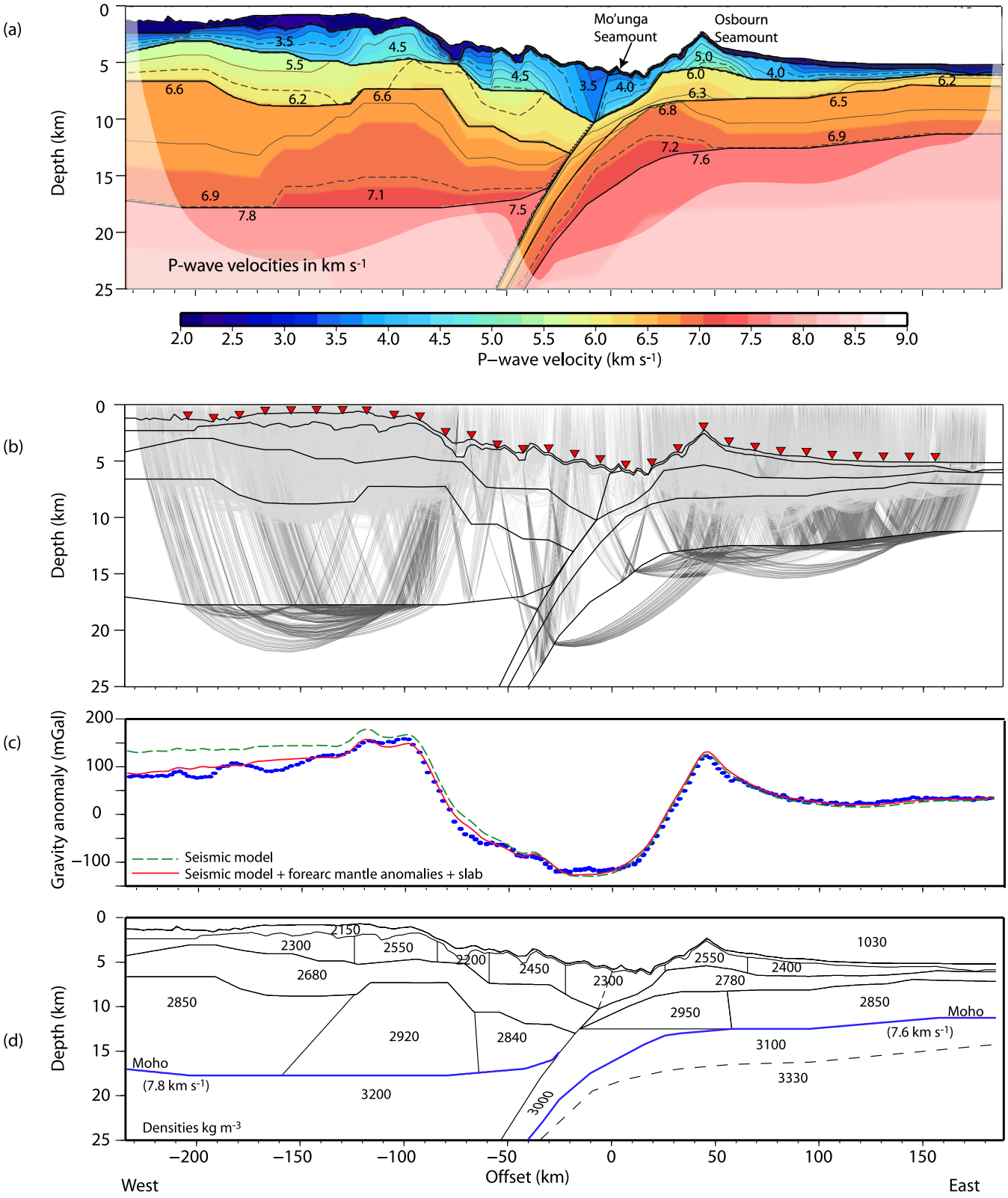

Figure 6. Modelling for Profile A. (a) Final velocity model. Labelled numbers are *P*-wave velocities in km s^{-1}. Lighter areas are not constrained by ray coverage. (b) Ray coverage. Light grey lines are P_g travel paths, darker grey are P_n and P_mP. Inverted triangles represent OBS locations. (c) Free-air gravity anomaly. Blue dots show the observed anomaly. The green line is the anomaly calculated from the crustal density model in (d) and the red line is the anomaly calculated from the crustal density model in (d) plus the subducted slab and low mantle densities below the forearc. (d) Density model derived from the crustal structure of the final velocity model (a), with densities annotated in kg m^{-3}. Blue lines show the Moho on each plate. Dashed line is depth to which lower P_n velocities are observed.

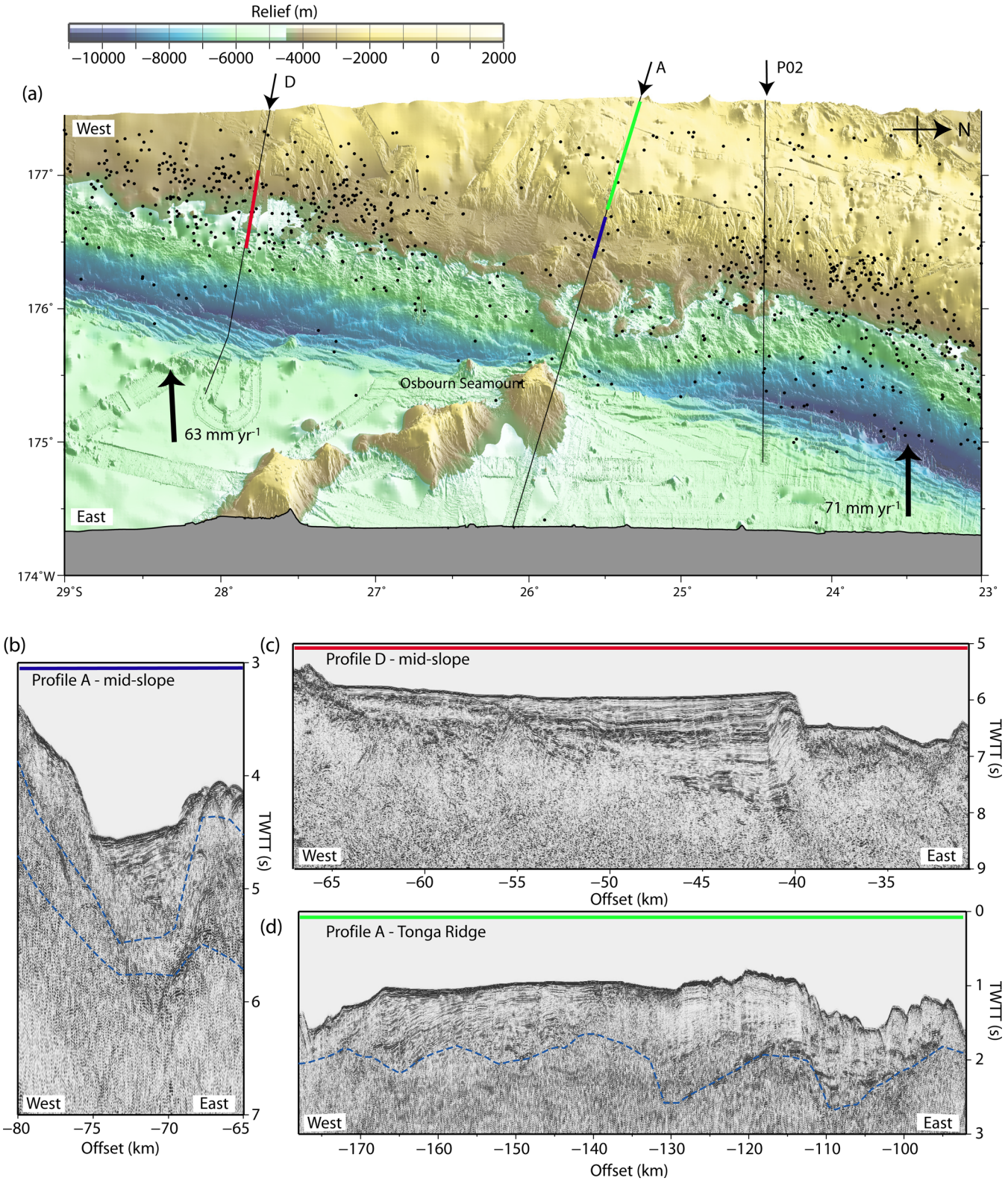

Figure 7. Comparison of forearc structures. (a) Seabed relief of the Tonga-Kermadec Trench–Louisville Ridge collision zone. Note the broad zone of deformation in the lower-trench slope in the centre of the collision zone, and the smoother lower-trench slopes to the north and south. Coloured lines are locations of MCS data in (b), (c) and (d). Black dots are background seismicity for earthquakes $>M_w = 5$. Numbered arrows show the plate motion vector. (b) Enlarged section of MCS data for the mid-slope basin on Profile A. Blue dashed lines are the layer interfaces from the final wide-angle model (Fig. 6a) converted to TWTT. (c) Enlarged section of MCS data for mid-slope basin on Profile D (Funnell *et al.* 2014). (d) Enlarged section of MCS data for Tonga Ridge sediment imaged on Profile A. Blue lines are the interfaces from the final wide-angle model (Fig. 6a) converted to TWTT.

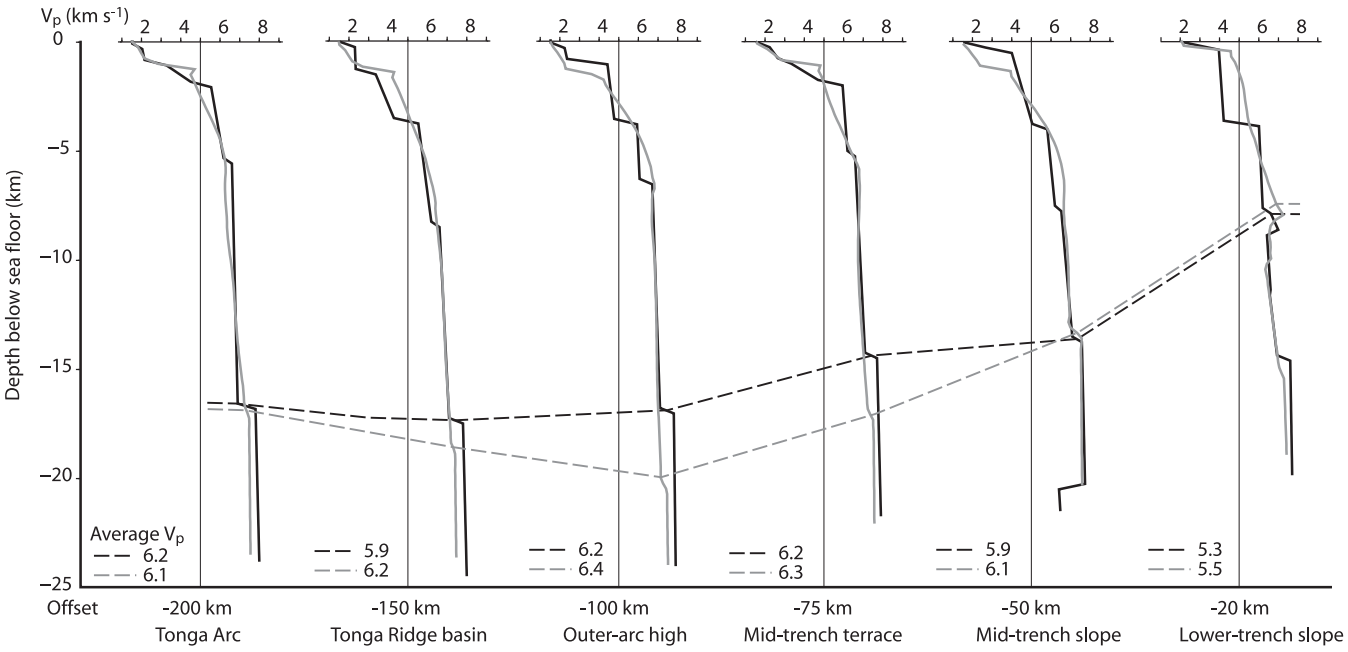

Figure 8. One-dimensional velocity profiles through the wide-angle models of Profiles A and P02. Velocity profiles are plotted with depth below seafloor. Offsets refer to offsets in Figs 9(b) and (d). Black lines are Profile A, grey lines are Profile P02. Dashed lines show the Moho location. Numbers at the bottom of each profile are average crustal V_p values for each 1D profile. Note the difference in crustal velocity between Profiles A and P02 in the 1–4 km depth range on the lower-trench slope.

resulting from dewatering and phase changes with increasing pressure and temperature (e.g. Hacker *et al.* 2003).

A good fit to the observed free-air anomaly was achieved without adjusting the seismically well-constrained part of the model, only by assigning the forearc mantle, between 100 and 300 km depth, a density contrast of –20 kg m^{-3} over a ∼500-km-wide region (–30 kg m^{-3} between 25 and 100 km depth). This is consistent with previous geodynamic models of the Tonga subduction zone which also require a broad region of low density in the mantle wedge (–20 kg m^{-3}), extending hundreds of kilometres west of the trench, to model the seafloor topography (Billen *et al.* 2003).

4 INTERPRETATION OF PROFILE A

We describe the final, best-fitting wide-angle model for the collision zone (Profile A — Fig. 6b) by tectonic section, west-to-east, from the Tonga Platform to the Pacific Plate. In addition, lateral variations in velocity layer and crustal thicknesses, and average velocities, between the arc and the trench are highlighted with a series of 1-D velocity–depth profiles, spaced at 25–50 km intervals (Fig. 8).

4.1 Tonga platform

An up to 1500-m-thick sequence of Oligocene-Recent volcaniclastics, pelagic chalks and carbonates with velocities of 2.0–2.5 km s^{-1} is deposited on the Tonga Ridge. These sediments undulate in thickness above a basement surface that is offset on steep normal faults (Fig. 6b). Extensional collapse towards the backarc is observed in tilting of sediment layers in the west (Fig. 6b, –200 to –170 km). Beneath the outer-arc high the basement is extended by small-scale distributed faulting (Fig. 6b, offsets –115 to –95 km) which most likely post-dates the deformation on the rest of the ridge (Fig. 6b, –170 to –115 km), as the resulting accommodation space is not yet sediment filled. The forearc crystalline crust comprises an Eocene basement where *P*-wave velocities are 3.5–4.5 km s^{-1}, increasing to 4.0–5.0 km s^{-1} beneath the outer-arc high (Fig. 6a). Basement velocities are slow on the western side of the ridge, where V_p of ∼5.5 km s^{-1} extends to ∼7 km depth. Average velocity in the middle and lower crust decreases by 0.3 km s^{-1} from east-to-west (Fig. 8), indicating a change in crustal structure across the ridge. The Moho depth is constrained by reversed P_n arrivals (V_p ∼ 7.8 km s^{-1}) from the mid-trench slope arcward and is 18 ± 1 km.

4.2 Trench slope

Sediment is transported eastward from the Tonga Ridge to a ∼12-km-wide mid-slope basin via a broad and shallow, ∼50-km-wide, series of trench-perpendicular canyons (Figs 9c and d, offset −80 km). The basin is the only region in the trench where a significant accumulation of sediment is identified on the MCS data (Fig. 2b, offset –75 km) and has two distinct units: (i) an upper ∼2-km-thick unit with distinct depositional layers and (ii) a lower, diffusely reflective unit. These two units most likely represent different phases of extension. The mid-slope basin is located above a sharp, ∼3 km increase in the depth to the >6.0 km s^{-1} middle and >6.5 km s^{-1} lower crust. These lateral changes in velocity structure demonstrate the full crustal scale of the present extensional deformation of the forearc.

The ∼60-km-wide lower-trench slope has a shallow angle and rapid lateral variation in seafloor relief (Fig. 9c). A ∼2 km topographic high in the centre of the slope (Fig. 6a, offset –35 km) is flanked to the east, north and south by basins and to the northeast and southwest by ramparts, where relatively low velocities (3.5–4.0 km s^{-1}) extend to ∼5 km beneath the seafloor. The high has a velocity of 4.0 km s^{-1} at the seafloor increasing to 5.5 km s^{-1} by 6 km depth (Fig. 9d). While of higher velocity in the near surface compared to the east and west, in the middle crust the <6 km s^{-1}

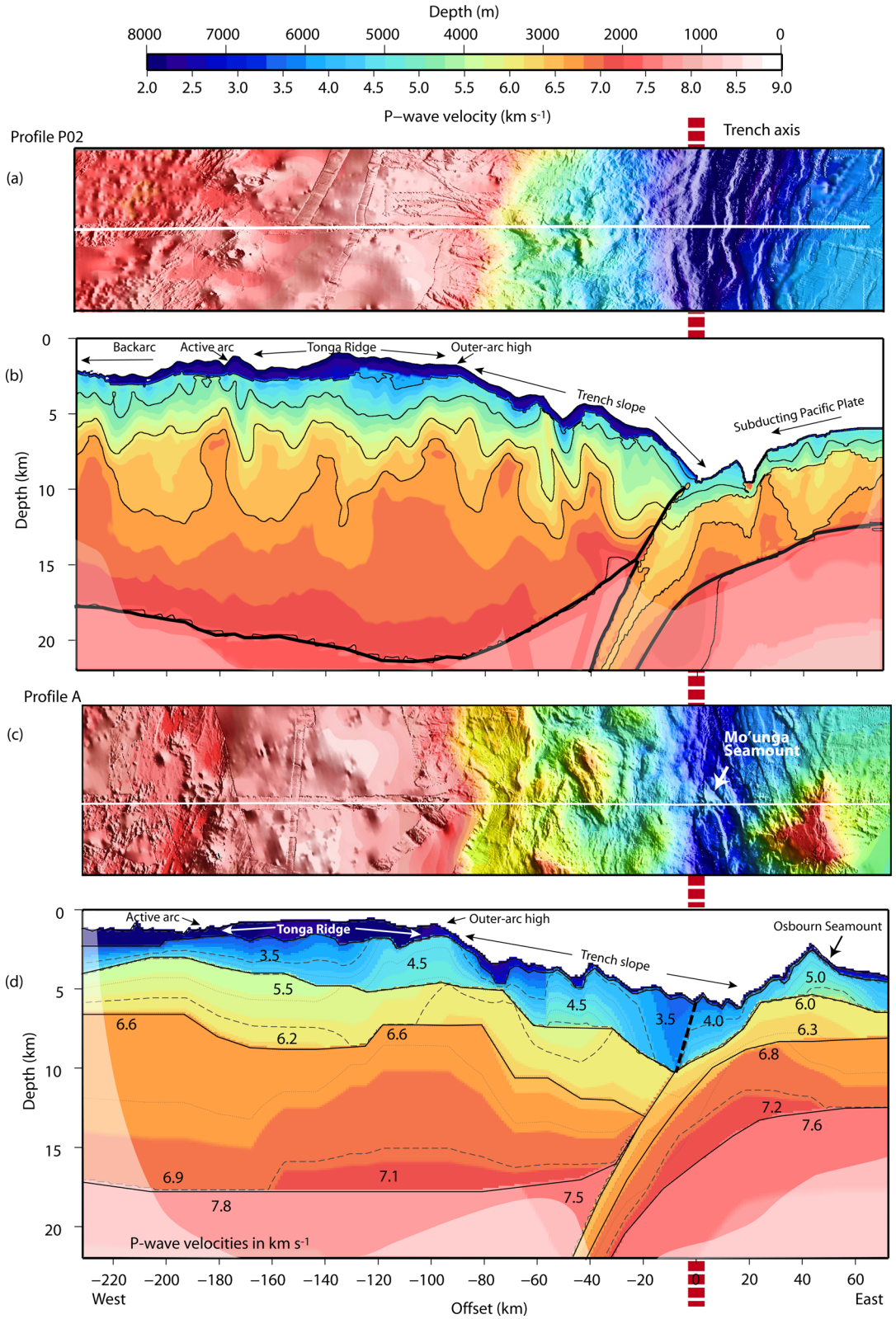

Figure 9. Comparison of wide-angle models. (a) Bathymetry along Profile P02. (b) Profile P02 final velocity model from the post-collision zone (Contreras-Reyes *et al.* 2011). Seamount subduction is inferred to have occurred here ∼0.5–1 Ma (Ruellan *et al.* 2003). (c) Bathymetry in the collision zone, along Profile A. (d) Final velocity model for Profile A. *P*-wave velocities are annotated in km s^{-1}. The location of the trench fault (Fig. 2d, inset) is marked with a black, dashed line. Red dashed lines on all parts show the trench axis.

velocity zone extends to a greater depth beneath the edifice than its surrounds.

4.3 Trench axis and the plate boundary

The trench floor on Profile A is ∼3 km shallower than to the north and south, and is congested with material carried into the trench on the subducting plate and by material of forearc provenance. The subducting, ∼10 km wide, Mo'unga Seamount (Pointoise *et al.* 1986; Ballance *et al.* 1989) creates a disparity between the geomorphic and tectonic trench axis locations and broadens the trench floor (Figs 6b, 9c and d). The geomorphic trench, the deepest part of the collision zone, is east of the seamount at the base of a graben that forms part of a region of extensional faulting on the seaward wall of the subducting Pacific Plate (Fig. 9c). The true plate boundary lies on the arcward side of the seamount, where a fault separates the forearc from trench fill originating from the Pacific Plate (Fig. 6b, inset), and can be traced ∼20 km to the west. Small-scale thrust faulting intersects the seafloor (Fig. 6b inset, offset –10 km) 10 km west of the fault on the arcward side of the ramparts of low-velocity material.

At the plate boundary, the forearc crustal thickness is estimated to be ∼12 km (including sediment and low V_p deformed forearc rock) where it abuts the subducting Pacific Plate, and the downdip plate interface width is ∼26 km (Fig. 8d). Although poorly constrained, decreasing upper mantle velocities in the mantle wedge below this part of the outer forearc to 7.5 km s^{-1}, where P_mP and P_n arrivals cross between the subducting and overriding plates (Figs 5a and b, offsets –30 to –60 km), improves the model fit to the long travelpath arrival times.

4.4 Osbourn Seamount

Outer-rise bend faults on the subducting Pacific Plate trend subparallel to the trench strike on the north side of Osbourn Seamount becoming more parallel to the south (Fig. 9c). The vertical relief across these faults is ∼200 m and they cut through the western flank of the seamount and down-step it into the trench. The outer trench wall is pervasively faulted with a 3- to 4-km-thick layer of velocity 3.5–4.5 km s^{-1} extending to ∼4 km beneath seafloor (Fig. 9d). These velocities suggest that material entering the trench here is not composed of low-velocity pelagic sediment, but is predominantly of seamount origin and most likely comprises lavas, volcanic breccia and volcaniclastic sediments. This material is inferred to be highly fractured and fluid saturated, both of which may contribute to the low velocities observed (Moos & Zoback 1983).

The summit of Osbourn Seamount has a ∼200-m-thick veneer of sediment with velocities of ∼2 km s^{-1}. On the eastern side of the edifice (Fig. 5a, offsets 60–120 km) the sediment layer thickens and velocities increase to 3.0 km s^{-1} at its base. Due to the low accumulation rates of pelagic material (Burns *et al.* 1973; Lonsdale 1986; Menard *et al.* 1987; Zhou & Kyte 1992; Heuret *et al.* 2012), and its semistratified nature, this layer is most likely predominantly composed of primary and reworked (mass wasting) volcaniclastic products from the seamount. Velocities within the seamount edifice are 4.5–5.5 km s^{-1}, which are representative of volcanic rock of basaltic composition (Christensen & Mooney 1995). In the middle crust velocities are 6.4–6.5 km s^{-1} (Fig. 6a, offsets 20–60 km), compared to >6.6 km s^{-1} of the oceanic crust to the east. The middle crust beneath the seamount shoals, tilts arcward, thickens, and has an apparent offset to the west. Similarly, a ∼30-km-wide region of high V_p (∼7.1 km s^{-1}) lower crust also has an apparent offset to the west. This offset may be due to the strike of the seismic profile being to the north of the seamount summit and/or the tilting and mass wasting of the low V_p volcaniclastics that cover the seamount as it enters the trench.

Beneath the seamount a crustal thickness of 8.0 ± 0.5 km is modelled, where crustal thickness is measured from the 6 km s^{-1} isovelocity contour (Fig. 6a). This is ∼2 km thicker than standard oceanic crust (White *et al.* 1992) and is predominantly attributable to the addition of volcanic material in the upper crust. Less than 500 m of crustal thickness may be attributed to underplating or significant thickening of the lower crust.

4.5 Pacific Plate

Volcaniclastics from Osbourn Seamount cover the Pacific Plate to the east end of the seismic profile (Fig. 5d). However, below the volcaniclastics magmatic alteration of the crust is not evident in the seismic velocity structure at offsets greater than 80 km east of the summit where velocities return to those of typical oceanic crust. Pacific Plate crust here is modelled from reversed P_n arrivals and has an average oceanic crustal thickness (White *et al.* 1992) of ∼6.5 ± 0.5 km (Fig. 6a). Moho geometry is constrained by reversed P_n arrivals between offsets of 20–170 km and upper mantle velocities are low at ∼7.6 ± 0.1 km s^{-1}. The travel paths of the P_n diving waves only sample the upper mantle to only ∼5 km depth beneath the Moho (Fig. 6b). Therefore, the full extent of the low P_n velocity region cannot be constrained from the wide-angle data alone. However, gravity modelling indicates that the low velocity, and hence low density, region beneath the subducting plate may not reach a significant depth, as a reduction in upper mantle density beneath this region is not required to fit the free-air anomaly (Figs 6c and d, offsets 0–150 km).

Although only observed over short offset ranges and with long travel-paths in the less-well constrained outer forearc lower crust, P_mP arrivals provide some constraint on the depth and geometry of the subducting plate Moho (Figs 6a and b, offsets –35 to –15 km). Moreover, combined with the low-density of the mantle wedge, this subducted slab geometry extrapolated to depth also produces a good fit to the amplitude and wavelength of the free-air anomaly of the forearc (Fig. 6c).

5 DISCUSSION

To characterize the mode of deformation of the subducting and overriding plates when undergoing seamount subduction (Profile A), and the north-to-south migration of this deformation along the forearc, results from previous studies in pre- and post-collision zones are used for comparison. Results from SO215 MCS profile D recorded ∼150 km to the south (Fig. 2d; Funnell *et al.* 2014) highlights the pre-collision zone, Kermadec subduction, structures. Approximately 150 km to the north, a traveltime inversion model produced by Contreras-Reyes *et al.* (2011) of wide-angle data acquired during a previous R/V Sonne cruise (SO195a) highlights the post-collision zone structures of Tonga subduction (Figs 1 and 9b, Profile P02).

5.1 Pre-collision zone

Distinct changes in the shape of the ridge and trench slope occur between the Tonga and Kermadec sections of the subduction zone. In contrast to the flat-topped Tonga Ridge, south of the collision zone

the Kermadec Ridge is narrow and the arc and ridge are co-incident. The trench-slope here is ∼160 km wide with a shallowly dipping upper-trench slope. Although this region is south of the Louisville Ridge collision zone, changes forearc structure over a broad region is evident in the bathymetry data with the ridge broadening from here into the collision zone (Fig. 2). A bathymetric high in the middle of the trench slope is not observed south of Profile D (Fig. 2c) but may be semi-continuous to the north merging with the outer-arc high on Profile A (Funnell *et al.* 2014). This feature along with the inferred uplift of the Kermadec forearc (Ruellan *et al.* 2003) may indicate that the structural changes evident between the northern Kermadec Ridge and the southern Tongan Ridge (i.e. from the pre- to current collision zone) are transitional between these two profiles. This transition in ridge structure between the collision and pre-collision zones may be due to pre-existing forearc structures. Alternatively, the deformation may be related to the far field effects of subduction of the thickened crust of the Louisville Ridge at the trench, although the ∼150 km distance south of the seamount flexural moats makes this less likely.

Tectonic erosion of the overriding plate in the pre-collision zone is inferred as subduction of the Pacific Plate at the Tonga-Kermadec Trench is fast (DeMets *et al.* 1994) and sediment poor (Heuret *et al.* 2012) with graben on the outer rise having little sediment fill (Profile , Fig. 2d; Funnell *et al.* 2014). Moreover, previous multichannel seismic reflection lines in the area image horst and graben structures on the Pacific Plate subducted below the outer forearc (von Huene & Scholl 1991). Formed in response to increased flexure and curvature of the subducting plate at the outer rise, the graben create a rough plate surface which can erode the overriding plate and deform the forearc (Hilde 1983; Ballance *et al.* 1989). Tectonic erosion is thus a normal feature of this plate boundary (Clift & MacLeod 1999) and is evidenced by extensional deformation across the mid- and lower-trench slopes (Fig. 7c). The down-faulting of the east side of the mid-slope terrace, which has left exposed sediments on the footwall (Fig. 7c; Funnell *et al.* 2014) and extensional collapse of the steep lower-trench slope at the trench (Fig. 2d) indicate that the forearc in the pre-collision zone is extending across most of the trench slope and undergoing gravitational collapse (von Huene & Scholl 1991; Stern 2011).

5.2 Collision zone

On the broad, elevated, and flat-topped Tonga Ridge sediment deposition rates and layer thicknesses vary with time (Herzer & Exon 1985; Tappin *et al.* 1994) and record the tectonic history of the ridge that proceeded from the initial subduction initiation to uplift associated with the opening of the backarc. A more recent uplift event in the Quaternary (Tappin *et al.* 1994) attributed to the subduction of the Louisville Ridge Seamount chain is also inferred (Herzer & Exon 1985). Although this uplift is inferred to be minor, only ∼300 m at most (Clift 1994). The ridge is currently ∼300 m higher than in the post-collision zone to the north and the Kermadec Ridge to the south and it terminates in the east against a steep upper-trench slope. A deformation front at the upper-trench slope—outer-arc high transition is inferred, separating stable ridge from the extending trench slope. However, the outer-arc high also has distributed small-scale extensional faulting (Fig. 7d, offset −100 km) and unlike the rest of the ridge on Profile A, the accommodation space produced by this faulting has not yet filled with sediment indicating that the deformation may also be moving arcward.

A major change in stress regime on the mid-trench slope is inferred from MCS data acquired across other subduction zones (von Huene & Culotta 1989). In the collision zone, isovelocity contours in the middle crust step down towards the trench indicating (Fig. 9d) the scale of the present extensional deformation. In addition, block faulting across the mid-trench slope offsets the seafloor with high relief. A ∼2-km-high block with similar velocities to that of the Eocene arc crust is interpreted as a fragment of the old arc that has slumped into the trench (Fig. 9d offsets –45 to –35 km), with the lower velocities beneath the block indicating extension of the trench slope crust. The high may be elevated due to underplating beneath the trench slope of subducted sediment, seamount derived material or the eroded outer forearc (Fisher *et al.* 1998; Sak *et al.* 2009).

The Moho beneath the mid- and upper-trench slope overlies mantle wedge where serpentinization is expected, and where reflectivity from the base of the crust is not observed. The seismically opaque zone is of a similar width (∼60 km) to the serpentinized zone in the Cascadian forearc and at most other Pacific Rim subduction zones (Bostock *et al.* 2002; Brocher *et al.* 2003; Hyndman & Peacock 2003). This is also in-keeping with observations from other Pacific Rim subduction zones where the Moho is either inverted, attenuated or absent due to serpentinization (Bostock *et al.* 2002; Brocher *et al.* 2003; Oakley *et al.* 2008; Stern 2011; Cheng *et al.* 2012). Serpentinization of the mantle wedge is produced by dewatering of subducted sediment and oceanic crust, and may contribute to a blurring of the boundary between crust and mantle (Brocher *et al.* 2003) and a combined reduction in lower crust and upper mantle velocity may occur (Fig. 6b). In the proximity of the plate boundary interface blurring of the Moho interface may also be enhanced by basal erosion by rough topography on the subducting plate (Clift & Vannucchi 2004).

Low velocity, fluid-filled trench deposits subducted beneath the forearc can contribute to basal erosion (Clift & Vannucchi 2004) and in the current collision zone this trench fill is largely supplied by the deforming Osbourn seamount. Small-scale faults imaged by swath mapping of its summit (Lonsdale 1986) and mass wasting of material from its western flank suggest that the edifice is deforming. As only thin accumulations of sediment are observed on the subducting Pacific Plate, the dominant sources of material entering the trench are inferred to be from these faulted flanks.

On the eastern side of Osbourn Seamount a semi-continuous reflector in the MCS data, interpreted as the top of the oceanic crust prior to seamount loading, can be traced to 160 km offset where it merges with the reflector of unloaded oceanic crust (Figs 5d and 10). This reflector shows the extent of the seamount moat and a flexural bulge is observed at its seaward termination (Fig. 6a). The distance between the seamount and the crest of the bulge is ∼110–120 km and suggests an elastic thickness of ∼10 km, consistent with its formation on relatively young oceanic crust at or near a mid-ocean ridge (Watts 1978).

Middle crustal rocks also shoal to the east (Fig. 6a) and suggest the flexural moat formed in response to seamount loading (Watts & Ribe 1984; Watts *et al.* 1997), which is also observed at Louisville Seamount further to the east in the chain (Contreras-Reyes *et al.* 2010). The main difference is that the moat infill dips towards Louisville Seamount but away from Osbourn Seamount. We infer this difference arises because Osbourn Seamount is presently 'riding' the Tonga-Kermadec outer rise, which has elevated both the seamount and its flanking moats. The flat summit of the seamount is tilted westward by ∼2.5° as it is carried over the outer rise.

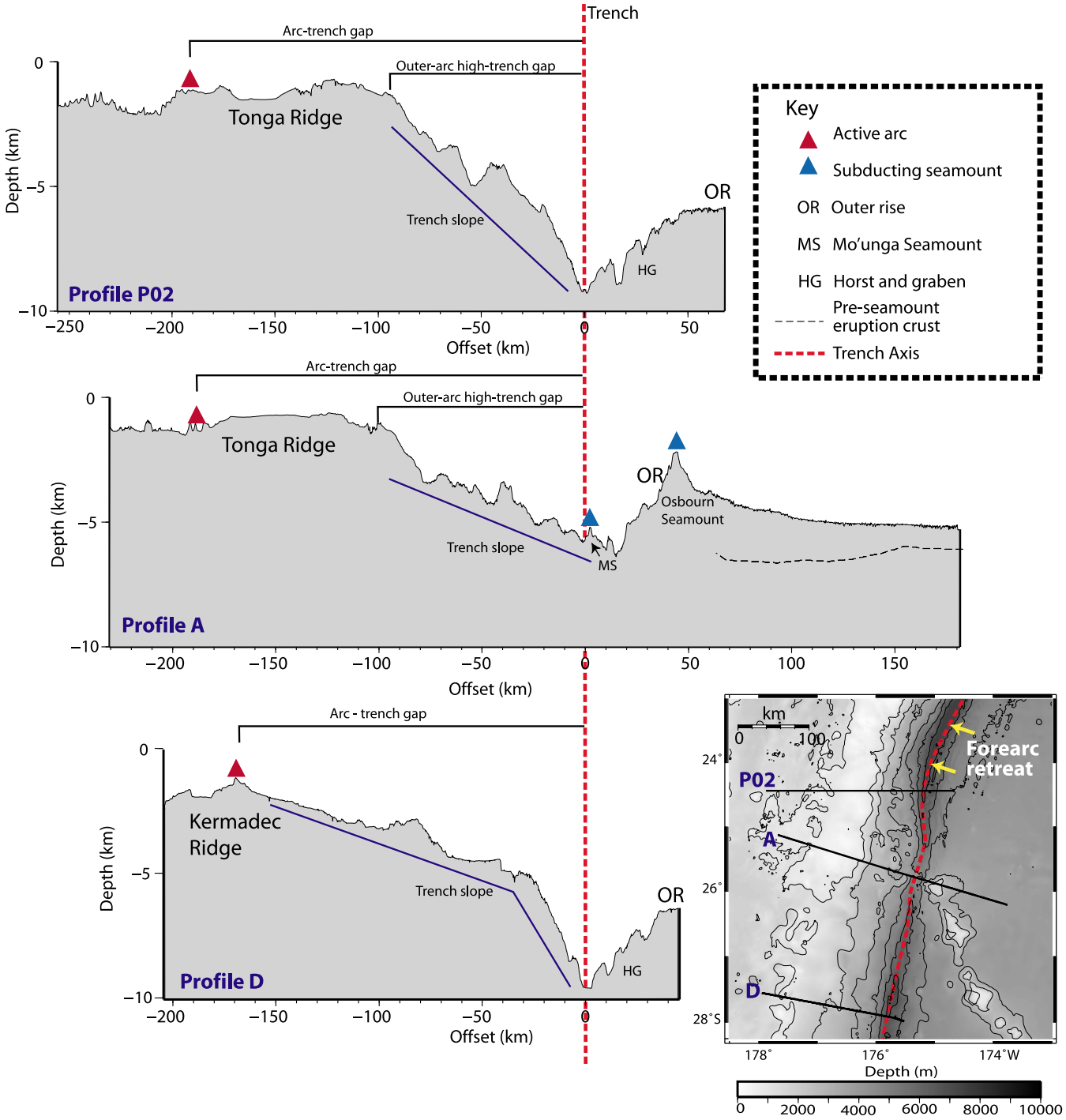

Figure 10. Summary of along-arc variation in the geomorphic features. Along-arc variation in forearc structures of the Tonga-Kermadec subduction zone have long been attributed to the subduction of the Louisville Ridge (Herzer & Exon 1985). Bathymetric data are plotted along profiles to highlight the main along-arc structural changes. Note the decrease in arc-trench gap between the Tonga and Kermadec Ridges. The outer-arc high–trench gap decreases between Profiles P02 and A, indicating greater erosion of the forearc in the north of the study area. Note the changes in the steepness and shape of the trench slope along the arc. Yellow arrows on the map show direction of forearc retreat. Red dashed line is location of the trench.

Upper mantle velocities beneath the outer rise are 8 per cent lower than those observed beneath the seamount chain to the east (Contreras-Reyes *et al.* 2010). These reduced mantle velocities are indicative of either serpentinization (Contreras-Reyes *et al.* 2011; Hyndman & Peacock 2003) or anisotropy (Savage 1999) and are modelled here to at least 150 km seaward of the trench. The broad zone over which the reduced mantle velocities are observed may indicate the extent over which bending related stresses act on the oceanic lithosphere as it passes over the outer rise.

5.3 Post-collision zone

Seamount subduction is inferred to have occurred in the post-collision zone at ~0.5–1 Ma (Ruellan *et al.* 2003). The ridge here

is ∼100 m deeper and trench-perpendicular canyons transport sediment from the Tonga Ridge towards the trench (Fig. 7a). These canyons feed sediment into two small, ∼1-km-deep, sediment-filled basins formed oblique to the trench on the mid-trench slope (Fig. 9a, offsets –50 and –70 km). A region of ∼0.3 km s^{-1} lower velocities (Fig. 7a — offsets of –40 and –70 km), compared to the Tonga Ridge basement, extends to ∼7 km depth in the crust indicating distributed deformation of the mid-trench slope. Compared to the collision zone, there is an observed decrease in trench slope relief, and increase in trench slope angle, although block faulting structures and seafloor relief still exceed 1 km (Figs 9a and c). In contrast to the collision zone, the lower-trench slope is a smooth, steep transition from the basins of the mid-slope down to the trench axis.

Seismic velocities in the near surface of the trench are ∼1 km s^{-1} faster in the post-collision zone and are thus, less likely to be due to seamount derived material. The trench is devoid of significant relief (Fig. 9a), and is comprised of a 6-km-thick zone of relatively low velocity (∼5.5 km s^{-1}) above the plate boundary (Figs 8 and 9b). A large part of the forearc crust here is interpreted to be of this low velocity material (Contreras-Reyes *et al.* 2011). A lower crust of velocity 6–7 km s^{-1} comprises the remaining 5 km, resulting in a total crustal thickness of only ∼9 km in the plate boundary zone and a downdip plate interface width of ∼21 km (Fig. 9b; Contreras-Reyes *et al.* 2011), a 3 km decrease in crustal thickness and 5 km decrease in plate boundary interface width compared to the collision zone. These structures and the reduction in crustal and plate interface width in the post-collision zone are indicative of a greater degree of extensional collapse of the trench slope and its increases in steepness indicates that the forearc may be eroding back to its pre-collision geometry (Lallemand *et al.* 1992).

As in the pre-collision zone to the south, away from the influence of the seamount chain, the subducting Pacific Plate has generally trench-parallel normal faults on the seaward wall of the trench with vertical offsets as high as 1.5 km with horst and graben widths up to 10 km (Fig. 2d). A zone of relatively low upper crustal velocities of (V_p = 4.0–5.5 km s^{-1}) extends to ∼3 km beneath the seafloor (Fig. 9b, offsets –30 to 0 km). Moreover, lower velocities are interpreted in the mid-crust beneath outer rise graben (Fig. 9b, V_p of 6.0–6.2 km s^{-1}, offsets 10–20 km) and in the mantle wedge (Fig. 9b, V_p of 7.3–7.5 km s^{-1}) and are inferred to result from pervasive faulting and serpentinization from deep penetrating fluids (Contreras-Reyes *et al.* 2011). In the collision zone, alteration of the crust due to Louisville Ridge magmagenesis likely masks the full extent of extensional deformation of the oceanic crust as it passes over the outer rise. In the post-collision zone, however, the extent of the deformation is evident in reduced velocities from the seafloor to the upper mantle (Contreras-Reyes *et al.* 2011).

5.4 Southward migrating seamount subduction

Migration of depocentres from north-to-south along the forearc has been attributed to the sequential uplift of the Tonga Ridge north of the study area, in response to the southward progressing Louisville Ridge subduction (Austin *et al.* 1989). Previous studies have concluded that seamount subduction is recorded as an angular unconformities within the sediment of perched basins located on the forearc (Clift *et al.* 1998). A progressive trenchward increase in dip of forearc sediment with depth beneath seafloor is measured at ODP site 841 at 23.3°S (Fig. 1) and interpreted to reflect basal erosion and progressive rotation of the forearc towards the trench. At this site, an increase in rotation rate at 0.5 Ma is attributed to collapse of the forearc in the wake of subduction of the Louisville Ridge (MacLeod 1994; Clift & MacLeod 1999). However, a period of arcward rotation of sediments during seamount collision with the trench is also inferred from changes in dip angle between pre- and post-collision sediment (MacLeod 1994; Clift *et al.* 1998). In the context of the above interpretation, we suggest that the arcward-tilted sediment in the mid-slope basin on Profile A records the onset of seamount subduction at the trench in the current collision zone. As the sediment is tilted arcward at a small angle and is not overlain by flat-lying deposits, this rotation is most likely a recent event.

Around 135 km of forearc erosion is inferred to have occurred at the Tonga Trench since the Eocene, of which, ∼80 km is attributed to subduction of the Louisville Ridge (Clift & MacLeod 1999). Thus, erosion due to seamount subduction is likely a significant contributor to the ∼80 km lateral offset in the trench at ∼23.5°S (Figs 1 and 10). Just to the north of this offset in trench is Horizon Deep, the deepest part of the Tonga Trench, where seafloor depths exceed 10.5 km (Fig. 1). Exposure of the surface of the subducting slab at the great depths of the trench here has been attributed to an increase in slab dip compared to the north (Billington 1980; Lonsdale 1986), and the westward retreat of the forearc (Wright *et al.* 2000) due to erosion in the wake of seamount subduction around 2–3 Ma (Lonsdale 1986; Pelletier & Dupont 1990; Ruellan *et al.* 2003).

At ∼23°S near Horizon Deep (Fig. 1), the absence of deep canyons is used to infer substantial collapse of the inner-trench slope due to the subduction of the ridge (Wright *et al.* 2000). This area is yet to re-establish the block faulting and canyon exploiting trench-perpendicular faults that are generally observed along the erosive Tonga-Kermadec margin (Wright *et al.* 2000), with the slope here having little relief (Figs 1 and 7a). A return to rough relief on the trench slope occurs south of ∼24.5°S and is co-incident with an eastward rotation in trench strike, the northern extent of the seismic gap and the approximate extent of the flexural moat of Louisville Seamount (Figs 1 and 10). The change in seismic state of the subduction zone to the south of ∼24.5°S may indicate that once seamounts have subducted beneath the forearc Moho, the region returns to a normal slip pattern (Scholz & Small 1997; Singh *et al.* 2011). It is unclear whether the change in seismogenesis reflects an unlocking of the plate interface or a reduction in aseismic stress release as the transfer of fluids to the overriding plate wanes or basal erosion of the overlying plate ceases (Singh *et al.* 2011).

Although located only 150 km north of Profile A, the smooth lower-trench slope and decrease in outer forearc crustal thickness and velocity on Profile P02 in the post-collision zone indicate a greater degree of extensional collapse. A reduction in bathymetric relief on the trench slope is observed at other subduction zones where high levels of extensional deformation of the forearc have occurred and is attributed to both gravity driven collapse producing distributed faulting, and the accumulation on the trench slope of mass-wasting debris from higher up the trench slope (von Huene & Ranero 2003). The trench axis–outer-arc high separation is 10 km less on Profile P02 than on Profile A (Fig. 10), which is in-keeping with observations of apparently missing crust and the retreat of the forearc at erosive margins (Lallemand *et al.* 1992; Fisher *et al.* 1998).

At the collision zone at ∼26°S, the trench shallows by 3 km as it becomes congested with incoming seamount-derived material and Mo'unga Seamount (Figs 7a and 10). Arcward rotation of the inner-trench slope by the impinging seamount is evidenced by the steepness of the plate boundary fault; the small-scale thrust faulting

that intersects the seafloor (Fig. 2b inset, offset –10 km) and the rampart of low-velocity material on the up-dip side of the fault (Fig. 2b and inset, offset –5 km). Relief increases on the inner-trench slope, and active deformation of the outer forearc is indicated by large-scale forearc blocks reaching 2 km in relief on the lower-trench slope, and sediment that records arcward rotation of the mid-slope basin.

Throughout the collision zone and to the south of the study area, the trench follows an approximately constant strike and rapidly regains a ∼9 km depth by 100 km south of Osbourn Seamount (Fig. 10). Profile D, ∼250 km south of Osbourn Seamount, images a deep, steep-sided trench, and the slab dip increases compared to the collision zone (Bonnardot *et al.* 2007; Hayes *et al.* 2012). As arc volcanoes are thought to form above a restricted depth range to the subducted slab (England *et al.* 2004), this increase in slab dip may be linked to the decrease in the arc-trench gap observed (Fig. 10). Although south of the Louisville Ridge collision zone and undergoing 'normal' Tonga-Kermadec subduction, faulting and sedimentation patterns on the forearc suggest that this region is also undergoing extensional collapse.

Where Louisville Ridge subducts however, a significant departure from this normal Tonga-Kermadec subduction is observed and an area of reduced trench depth and a broad and shallow sloped block-faulted outer forearc, demarks the ∼150-km-wide seamount collision zone. However, this departure may be transient and a rapid southward progression of the collision zone and the return to normal Tonga-Kermadec subduction is inferred from the short, ∼180 km along-arc transition from pre-seamount to post-seamount subduction forearc structures in as little as 1.5 Ma.

6 CONCLUSIONS

A synthesis of the seismic structure and seabed geomorphology along the Tonga-Kermadec subduction zone indicates a north-to-south progression in the degree of forearc deformation. In the current collision zone the key evidence for deformation during seamount subduction include:

(1) Subduction of Mo'unga Seamount, currently in the centre of the trench, broadens and shallows the trench floor and rotates the plate boundary fault arcward. The plate boundary lies on the west side of this seamount.

(2) A ∼ 5-km-thick region of ∼4 km s^{-1} material fills the trench to the east of Mo'unga Seamount. Mass wasting events off the west side of Osbourn Seamount likely supply a significant amount of the low V_p material to the trench.

(3) Elevated topographic blocks on the mid-trench slope may represent fragments of the Eocene arc that have slumped into the trench, with the lower velocities at depth reflecting extension of the trench-slope. The blocks may be elevated due to underplating beneath the lower-trench slope of subducted sediment, seamount derived material or the eroded outer forearc.

(4) The trench slope break is characterized by a ∼2 km fault scarp and a seafloor depth increase towards the trench. A ∼3 km increase in depth to the middle and lower crustal layers and a decrease in average V_p to 5.9 km s^{-1} occur beneath the mid-trench slope, indicating deformation throughout the crustal column.

(5) Recent deformation of the forearc is indicated by the arcward tilt of seafloor sediments in the mid-slope basin and the ∼300 m elevation increase of the Tonga Ridge in the collision zone, compared to the north and south.

Evidence for the north-to-south changes in forearc deformation due to seamount subduction include:

(1) Relief on the lower-trench slope is lower in the post-collision zone due to increased erosion in the wake of seamount subduction.

(2) The 10 km decrease in trench axis–outer-arc high separation at this location indicates the leading edge of the overriding plate is eroding arcward (west). A ∼80 km lateral offset in the Tonga-Kermadec Trench just south of Horizon Deep has been attributed to erosional retreat of the forearc in the wake of seamount subduction.

(3) Mid-slope basins in the pre-collision zone are more deformed than those observed to the south. Crustal velocities beneath these forearc basins suggest that extensional deformation extends into the upper crust. In the pre-collision zone in the south, the mid-slope is a broad basin of ∼3 km stratified sediments with only distributed small scale-extension.

(4) The edges of the seismic gap beneath the Tonga forearc roughly coincide with the approximate extent of the Osbourn Seamount flexural moat. Subduction of a seamount and its flexural moat beneath the forearc Moho may control the seismogenesis of the subducting plate, by either releasing the locking stresses, or by removing the source of fluids that may have facilitated aseismic slip on the plate interface.

ACKNOWLEDGEMENTS

We would like to thank all those involved in the data acquisition and instrument preparation for the RV Sonne SO215 cruise, including the officers and crew of the R/V Sonne, the scientific party, the sea-going technicians from the U.K.'s Natural Environment Research Council (NERC) National Marine Facility Sea Systems and Exploration Electronics Ltd. OBSs were provided by the NERC's Ocean-Bottom Instrumentation Facility (Minshull *et al.* 2004) and from IFM-Geomar with funding from the Ocean Facilities Exchange Programme assisted by Prof Ernst Flueh. The wide-angle data were modelled and plotted using programs written by Zelt & Smith (1992) and the MCS were processed using Globe Claritas. All figures were generated with the Generic Mapping Tools (Wessel & Smith 1991). This research project was funded by the NERC (grant reference NE/F004273/1) as a collaboration with the German funded project TOTAL (Tonga Thrust earthquake Asperity at Louisville Ridge) project (Peirce & Watts 2011). All SO215 raw data are archived at the NERC's British Oceanographic Data Centre. The final submitted version of this manuscript is available through Durham Research Online (dro.dur.ac.uk). We kindly thank David Scholl, Paola Vannucchi and two anonymous reviewers for helpful comments on this paper.

REFERENCES

Austin, J.A., Taylor, F.W. & Cagle, C.D., 1989. Seismic stratigraphy of the central Tonga Ridge, *Mar. Petrol. Geol.,* **6,** 71–92.

Ballance, P.F., Scholl, D.W., Vallier, T.L., Stevenson, A.J., Ryan, H. & Herzer, R.H., 1989. Subduction of a Late Cretaceous seamount of the Louisville Ridge at the Tonga Trench: a model of normal and accelerated tectonic erosion, *Tectonics,* **8,** 953–962.

Becker, J.J. *et al.*, 2009. Global bathymetry and elevation data at 30 arc seconds resolution: SRTM30_PLUS', *Mar. Geod.,* **32,** 355–371.

Billen, M.I., Gurnis, M. & Simons, M., 2003. Multiscale dynamics of the Tonga-Kermadec subduction zone, *Geophys. J. Int.,* **153,** 359–388.

Billington, S., 1980. The morphology and tectonics of the subducted lithosphere in the Tonga–Fiji–Kermadec region from seismicity and focal mechanisms solutions, *PhD thesis,* Cornell University.

Bloomer, S.H., Ewart, A., Hergt, J.M. & Bryan, W.B., 1994. Geochemistry and origin of igneous rocks from the outer Tonga forearc (site 841), in *Proceedings of the Ocean Drilling Program, Scientific Results,* eds Hawkins, J. *et al.*, Ocean Drilling Program, College Station, TX.

Bonnardot, M.-A., Regnier, M., Ruellan, E., Christova, C. & Tric, E., 2007. Seismicity and state of stress withing the overriding plate of the Tonga-Kermadec subduction zone, *Tectonics,* **26,** 1–15.

Bostock, M.G., Hyndman, R.D., Rondenay, S. & Peacock, S.M., 2002. An inverted continental Moho and serpentinization of the forearc mantle, *Nature,* **417,** 536–538.

Brocher, T.M., 2005. Empirical relations between elastic wavespeeds and density in the Earth's crust, *Bull. seism. Soc. Am.,* **95,** 2081–2092.

Brocher, T., Parsons, T., Tréhu, A., Snelson, C. & Fisher, M., 2003. Seismic evidence for widespread serpentinized forearc upper mantle along the Cascadia margin, *Geology,* **31,** 267–270.

Burns, R.E. *et al.*, 1973. Site 204, in *Initial Reports of the Deep Sea Driling Project 21,* Texas A & M University, O. D. P. DSDP Deep Sea Drilling Project, TX.

Cheng, W.B., Hsu, S.K. & Chang, C.H., 2012. Tomography of the southern Taiwan subduction zone and possible emplacement of crustal rocks into the forearc mantle, *Global Planet. Change,* **90–91,** 20–28.

Christensen, D. & Lay, T., 1988. Large earthquakes in the Tonga region associated with subduction of the Louisville Ridge, *J. geophys. Res.,* **93,** 13 367–313 389.

Christensen, N.I. & Mooney, W.D., 1995. Seismic velocity structure and composition of the continental crust: a global review, *J. geophys. Res.,* **100,** 9761–9788.

Clift, P.D., 1994. Controls on the sedimentation and subsidence history of an active plate margin, in *Proceedings of the Ocean Drilling Program, Scientific Results,* pp. 173–188, Ocean Drilling Program, College Station, TX.

Clift, P.D. & MacLeod, C.J., 1999. Slow rates of subduction erosion estimated from subsidence and tilting of the Tonga forearc, *Geology,* **27,** 411–414.

Clift, P.D. & Pecher, I., 2003. Tectonic erosion of the Peruvian forearc, Lima Basin, by subduction and Nazca Ridge collision, *Tectonics,* **22,** doi:10.1029/2002TC001386.

Clift, P.D. & Vannucchi, P., 2004. Controls on tectonic accretion versus erosion in subduction zones: implications for the origin and recycling of the continental crust, *Rev. Geophys.,* **42,** 1–31.

Clift, P.D., MacLeod, C.J., Tappin, D.R., Wright, D.J. & Bloomer, S.H., 1998. Tectonic controls on sedimentation and diagenesis in the Tonga Trench and forearc, southwest Pacific, *Bull. geol. Soc. Am.,* **110,** 483–496.

Clouard, V. & Bonneville, A., 2005. Ages of seamounts, islands and plateaux on the Pacific Plate, in *Plates, Plumes and Paradigms,* pp. 71–90, eds Foulger, G.R., Natland, J.H., Presnall, D. & Anderson, D.L., Geological society of America, Special paper.

Contreras-Reyes, E., Grevemeyer, I., Watts, A.B., Planert, L., Flueh, E.R. & Peirce, C., 2010. Crustal intrusion beneath the Louisville hotsopt track, *Earth planet. Sci. Lett.,* **289,** 323–333.

Contreras-Reyes, E., Grevemeyer, I., Watts, A.B., Flueh, E.R., Peirce, C., Moeller, S. & Papenberg, C., 2011. Deep seismic structure of the Tonga subduction zone: implications for mantle hydration, tectonic erosion, and arc magmatism, *J. geophys. Res.,* **116,** 1–18.

Crawford, W.C., Hildebrand, J.A., Dorman, L.M., Webb, S.C. & Wiens, D.A., 2003. Tonga Ridge and Lau Basin crustal structure from seismic refraction data, *J. geophys. Res.,* **108**(6-1), 6–9.

DeMets, C., Gordon, R.G., Argus, D.F. & Stein, S., 1994. Effect of recent revisions to the geomagnetic reversal time scale and estimates of current plate motions, *Geophys. Res. Lett.,* **21,** 2191–2194.

Dupont, J. & Herzer, R., 1985. Effect of subduction of the Louisville Ridge on the structure and morphology of the Tonga arc, in *Geology and Offshore Resources of Pacific Island Arcs—Tonga Region,* Circum-Pac. Counc. Energy Miner. Resour., Earth Science Series, Vol. 2, pp. 323–332, eds Scholl, D.W. & Valuer, T.L., Houston, TX.

England, P., Engdahl, R. & Thatcher, W., 2004. Systematic variation in the depths of slabs beneath arc volcanoes, *Geophys. J. Int.,* **156,** 377–408.

Expedition_330_Scientists, 2012. Expedition 330 summary, in *Proceedings of the IODP, 330: Tokyo (Integrated Ocean Drilling Program Management International, Inc.*), eds Koppers, A.A.P., Yamazaki, T., Geldmacher, J. & Scientists, E., Tokyo.

Fisher, D.M., Gardner, T.W., Marshall, J.S., Sak, P.B. & Protti, M., 1998. Effect of subducting sea-floor roughness on fore-arc kinematics, Pacific coast, Costa Rica, *Geology,* **26,** 467–470.

Fleury, J.-M., Pubellier, M. & de Urreiztieta, M., 2009. Structural expression of forearc crust uplfit due to subducting asperity, *Lithos,* **113,** 318–330.

Funnell, M.J., Peirce, C., Stratford, W.R., Paulatto, M. & Watts, A.B., 2014. Structure and deformation of the Tonga-Kermadec subduction system in the Louisville Ridge pre-collision zone, *Geophys. J. Int.,* **199,** 1286–1302.

Geist, E.L., Fisher, M.A. & Scholl, D.W., 1993. Large-scale deformation associated with ridge subduction, *Geophys. J. Int.,* **115,** 344–366.

Hacker, B.R., Abers, G.A. & Peacock, S.M., 2003. Subduction factory 1: theoretical minerology, densities, seismic wave speeds and H_2O contents, *J. geophys. Res.,* **108,** 2029, doi:10.1029/2001JB001127.

Hayes, G.P., Wald, D.J. & Johnson, R.L., 2012. Slab 1.0: a three-dimensional model of global subduction zone geometries, *J. geophys. Res.,* **117,** 1–15.

Herzer, R. & Exon, N., 1985. Structure and basin anaylsis of the southern Tonga forearc, in *Geology and Offshore Resources of Pacific Island Arcs—Tonga Region,* Circum-Pac. Counc. Energy Miner. Resour., Earth Science Series, Vol. 2, pp. 55–73, eds Scholl, D.W. & Vallier, T.L., Houston, TX.

Heuret, A., Conrad, C.P., Funiciello, F., Lallemand, S. & Sandri, L., 2012. Relation between subduction megathrust earthquakes, trench sediment thickness and upper plate stress, *Geophys. Res. Lett.,* **39,** 1–6.

Hilde, T.W.C., 1983. Sediment subduction versus accretion around the Pacific, *Tectonophysics,* **99,** 381–397.

Hyndman, R.D. & Peacock, S.M., 2003. Serpentinization of the forearc mantle, *Earth planet. Sci. Lett.,* **212,** 417–432.

Koppers, A.A.P., Duncan, R.A. & Steinberger, B., 2004. Implications of a non linear $^{40}Ar/^{39}Ar$ age progression along the Louisville seamount trail for models of fixed and moving hot spots, *Geochem. Geophys. Geosyst.,* **5,** Q06L02, doi:10.1029/2003GC000671.

Koppers, A.A.P. *et al.*, 2012. Limited latitudinal mantle plume motion for the Louisville hotspot, *Nat. Geosci.,* **5,** 911–917.

Lallemand, S.E., Malavieille, J. & Calassou, S., 1992. Effects of oceanic ridge subduction on accretionary wedges: experimental modeling and marine observations, *Tectonics,* **11,** 1301–1313.

Laursen, J., Scholl, D.W. & von Huene, R., 2002. Neotectonic deformatiom of the central Chile margin: deepwater forearc basin formation in response to hot spot ridge and seamount subduction, *Tectonics,* **21,** 2-1–2-27.

Lonsdale, P., 1986. A Multibeam Reconnaissance of the Tonga Trench Axis and its Intersection With the Louisville Guyot Chain, *Mar. Geophys. Res.,* **8,** 295–327.

Ludwig, W.J., Nafe, J.E. & Drake, C.L., 1970. Seismic refraction, in *The Sea*, pp. 53–84, ed. Maxwell, A.E., Wiley-Interscience, New York.

MacLeod, C.J., 1994. Structure of the outer Tonga Forearc at Site 841, in *Proceeding ODP, Sci. Results,* pp. 313–329, eds Hawkins, J. *et al.*, Ocean Drilling Program, College Station, TX.

Malahoff, A., Feden, R.H. & Dleming, H.S., 1982. Magnetic anomalies and tectonic fabric of marginal basins north of New Zealand, *J. geophys. Res.,* **87,** 4109–4125.

Menard, H.W., Natland, J.H., Jordan, T.H. & Orcutt, J.A., 1987. Site 596: hydraulic piston coring in an area of low surface productivity in the southwest Pacific, in *Initial Rreport,* ed. Party, L.S.S., DSDP 91.

Minshull, T.A., Sinha, M.C. & Peirce, C., 2004. Multi-disciplinary, subseabed geophysical imaging—a new pool of 28 seafloor instruments in use by the United Kingdom Ocean Bottom Instrument Consortium, *Sea Technol.,* **46,** 27–31.

Moos, D. & Zoback, M.D., 1983. In situ studies of velocity in fractured crystalline rocks, *J. geophys. Res.,* **88,** 2345–2358.

Oakley, A.J., Taylor, B. & Moore, G.F., 2008. Pacific Plate subduction beneath the central Mariana and Izu-Bonin forearcs: new insights from an old margin, *Geochem. Geophys. Geosyst.,* **9,** doi:10.1029/2007GC001820.

Parson, L.M. & Hawkins, J., 1994. Two-stage ridge propagation and the geological history of the Lau backarc basin, *Proc. Ocean Drill. Program. Sci. Results,* **135,** 819–828.

Peirce, C. & Watts, A., 2011. R/V Sonne SO215 — Cruise Report, The Louisville Ridge—Tonga Trench collision: implications for subduction zone dynamics. Department of Earth Sciences, Durham University, Durham.

Pelletier, B. & Dupont, J., 1990. Erosion, accretion, backarc extension and slab length along the Kermadec subduction zone, Southwest Pacific, *Comptes Rendu de l'Academie des Sciences* Paris Ser II, 1657–1664.

Pointoise, B. *et al.*, 1986. La Subduction del la ridge de Louisville le long de la tosse des Tonga: premiers resultats de la campagne SEAPSO (Leg V), *C.R. Seances Acad. Sci. Ser. II,* **11,** 911–918.

Ruellan, E., Lafoy, Y., Auzende, J.-M., Foucher, J.-P. & Dupont, J., 1994. Oblique spreading in the southern part of the Lau Back-Arc Basin (SW Pacific), in *Geology and Submarine Resources of the Tonga-Lau-Fiji Region,* pp. 319–327, eds Stevenson, A.J., Herzer, R.H. & Ballance, P.F., SOPAC Technical Bulletin, Suva, Fiji.

Ruellan, E., Delteil, J., Wright, I. & Matsumoto, T., 2003. From rifting to active spreading in the Lau Basin—Harvre Trough backarc system (SW Pacific): locking/unlocking induced by seamount chain subduction, *Geochem. Geophys. Geosyst.,* **4,** doi:10.1029/2001GC000261.

Sak, P.B., Fisher, D.M., Gardner, T.W., Marshall, J.S. & LaFemina, P.C., 2009. Rough crust subduction, forearc kinematics, and Quaternary uplift rates, Costa Rican segment of the Middle American Trench, *Bull. geol. Soc. Am.,* **121,** 992–1012.

Savage, M.K., 1999. Seismic anisotropy and mantle deformation: what have we learned from shear wave splitting studies, *Rev. Geophys.,* **37,** 65–106.

Scholz, C.H. & Small, C., 1997. The effect of seamount subduction on seismic coupling, *Geology,* **25,** 487–490.

Singh, S.C. *et al.*, 2011. Aseismic zone and earthquake segmentation associated with a deep subducted seamount in Sumartra, *Nat. Geosci. Lett.,* **1119,** 308–311.

Stern, C.R., 2011. Subduction erosion: rates, mechanisms, and its role in arc magmatism and the evolution of the continental crust and mantle, *Gondwana Res.,* **20,** 284–308.

Sutherland, R., 1999. Basement geology and the tectonic development of the greater New Zealand region: an interpretation from regional magnetic data, *Tectonophysics,* **308,** 341–362.

Talwani, M., Worzel, J.L. & Landisman, M.G., 1959. Rapid gravity computations for two-dimensional bodies with application to the Mendocino submarine fracture zone (Pacific Ocean), *J. geophys. Res.,* **64,** 49–59.

Tappin, D.R., 1994. *The Tonga Frontal Arc Basin,* pp. 157–176, Elsevier.

Tappin, D.R., Herzer, R.H. & Stevenson, A.J., 1994. Structure and history of an oceanic forearc—the Tonga Ridge—22° to 26° south, in *Geology and Submarine Resources of the Tonga-Lau-Fiji Region,* pp. 81–100, eds Stevenson, A.J., Herzer, R.H. & Ballance, P.F., SOPAC Technical Bulletin, Suva, Fiji.

Taylor, F.W. *et al.*, 2005. Rapid forearc uplift and subsidence caused by impinging bathymetric features: examples from the New Hebrides and Solomon arcs, *Tectonics,* **24,** TC6005, doi:10.1029/2004TC001650.

Trehu, A.M., Blakey, R.J. & Williams, M.C., 2012. Subducted seamounts and recent earthquakes beneath the central Cascadia forearc, *Geology,* **40,** 103–106.

von Huene, R. & Culotta, R., 1989. Tectonic erosion at the front of the Japan Trench convergent margin, *Tectonophysics,* **160,** 75–90.

von Huene, R. & Ranero, C.R., 2003. Subduction erosion and basal friction along the sediment-starved convergent margin off Antofagasta, Chile, *J. geophys. Res.,* **108,** doi:10.1029/2001JB001569.

von Huene, R. & Scholl, D.W., 1991. Observations at convergent margins concerning sediment subduction, subduction erosion, and the growth of continental crust, *Rev. Geophys.,* **29,** 279–316.

Wang, K. & Bilek, S.L., 2014. Invited review paper: fault creep caused by subduction of rough seafloor relief, *Tectonophysics,* **610,** 1–24.

Watts, A.B., 1978. An Analysis of Isostasy in the World's Oceans 1. Hawaiian-Emperor Seamount Chain, *J. geophys. Res.,* **83,** 5989–6004.

Watts, A.B. & Ribe, N.M., 1984. On geoid heights and flexure of the lithosphere at seamounts, *J. geophys. Res.,* **89,** 11 152–11 170.

Watts, A.B. & Talwani, M., 1974. Gravity anomalies seaward of deep sea trenches and their tectonic implications, *Geophys. J. R. astr. Soc.,* **36,** 57–90.

Watts, A.B., Weissel, J.K., Duncan, R.A. & Larson, R.I., 1988. Origin of the Louisville Ridge and is relationship to the Eltanian fracture zone system, *J. geophys. Res.,* **93,** 3051–3077.

Watts, A.B., Peirce, C., Collier, J., Dalwood, R., Canales, J.P. & Henstock, T.J., 1997. A seismic study of lithospheric flexure in the vicinity of Tenerife, Canary Islands, *Earth planet. Sci. Lett.,* **146,** 431–447.

Weissel, J.K., 1979. Evolution of the Lau Basin by the growth of small plates, in *Island Arcs Deep-Sea Trenches and Back-Arc Basins,* pp. 429–436, eds Talwani, M. & Pitman, W.C., American Geophysical Union.

Wessel, P. & Smith, W.H.F., 1991. Free software helps map and display data, *EOS, Trans. Am. geophys. Un.,* **441,** 445–446.

White, R.S., McKenzie, D. & O'Nions, R.K., 1992. Oceanic crustal thickness from seismic measurements and rare earth element inversions, *J. geophys. Res.,* **97,** 19 683–19 715.

Wright, D.J., Bloomer, S.H., MacLeod, C.J., Taylor, B. & Goodlife, A.M., 2000. Bathymetry of the Tonga Trench and forearc: a map series, *Mar. Geophys. Res.,* **21**, 489–512.

Zelt, C.A. & Smith, R.B., 1992. Seismic travel time inversion for 2-D crustal velocity structure, *Geophys. J. Int.,* **108,** 16–34.

Zhou, L. & Kyte, F.T., 1992. Sedimentation history of the South Pacific pelagic clay province over the last 85 million years inferred from the geochemistry of DSDP, *Paleoceanography,* **7,** 441–465.